

Searches for stochastic gravitational-wave backgrounds

Joseph D. Romano

Department of Physics

Texas Tech University, Lubbock, TX 79409

email: joseph.d.romano@ttu.edu

Les Houches Summer School

July 2018

Abstract

These lecture notes provide a brief introduction to methods used to search for a stochastic background of gravitational radiation—a superposition of gravitational-wave signals that are either too weak or too numerous to individually detect. The focus of these notes is on relevant data analysis techniques, not on the particular astrophysical or cosmological sources that are responsible for producing the background. The lecture notes are divided into two main parts: (i) an overview, consisting of a description of different types of gravitational-wave backgrounds and an introduction to the method of cross-correlating data from multiple detectors, which can be used to extract the signal from the noise; (ii) details, extending the previous discussion to non-trivial detector response, non-trivial overlap functions, and a recently proposed Bayesian method to search for the gravitational-wave background produced by stellar-mass binary black hole mergers throughout the universe. Suggested exercises for the reader are given throughout the text, and compiled in an appendix.

Contents

I Overview / Basics	4
1 Motivation	4
1.1 Gravitational-wave analogue of the cosmic microwave background	4
1.2 The background of BBH and BNS mergers in the LIGO band	5
2 Different types of stochastic backgrounds	7
2.1 Different sources	7
2.2 Different signal properties	8
3 Mathematical characterization of a stochastic background	10
3.1 Plane-wave expansion	11
3.2 Ensemble averages	12
3.3 Energy density spectrum in gravitational waves	13
3.4 Calculating $\Omega_{\text{gw}}(f)$ for an astrophysically-generated background	14
3.4.1 Example: $\Omega_{\text{gw}}(f)$ for binary inspiral	14
4 Correlation methods	15
4.1 Basic idea	16
4.2 Extension to multiple data samples	17
4.3 Optimal filtering	18
5 Optimal filtering applied to some simple examples	19
5.1 Single-component analyses	20
5.2 Multi-component analysis	20
II Details / Examples	22
6 Non-trivial detector response	23
6.1 Beam detectors and different types of detector response	23
6.2 Detector response functions	24
6.3 Examples	24
6.3.1 Detector response for a one-arm, one-way detector	24
6.3.2 Detector response for a laser interferometer in the short-antenna limit	27
7 Non-trivial correlations	28
7.1 Overlap function	29
7.2 Examples	30
7.2.1 Overlap function for a pair of laser interferometers in the short-antenna limit	30
7.2.2 Overlap function for pulsar timing arrays	31
7.2.3 Overlap function for a pair of electric dipole antennae	32

8 Statistical inference	34
8.1 Comparing frequentist statistics and Bayesian inference	34
8.1.1 Likelihood functions	35
8.2 Frequentist analyses	36
8.3 Bayesian analyses	37
8.3.1 Bayes factors and model selection	37
8.3.2 Bayesian signal priors	39
9 Searching for the background of binary black-hole mergers	40
9.1 Analysis details	41
9.2 Illustrating the analysis method on simulated data	42
9.3 Comparison with the standard cross-correlation search	44
10 Final thoughts	45
A Exercises	46
A.1 Rate estimate of stellar-mass binary black hole mergers	46
A.2 Relating $S_h(f)$ and $\Omega_{\text{gw}}(f)$	46
A.3 Cosmology and the “Phinney formula” for astrophysical backgrounds	47
A.4 Optimal filtering for the cross-correlation statistic	47
A.5 Maximum-likelihood estimators for single and multiple parameters	48
A.6 Timing-residual response for a 1-arm, 1-way detector	48
A.7 Overlap function for colocated electric dipole antennae	49
A.8 Maximum-likelihood estimators for the standard cross-correlation statistic	49
A.9 Derivation of the maximum-likelihood ratio detection statistic	49
A.10 Standard likelihood marginalizing over stochastic signal prior	50

Part I

Overview / Basics

In the first part of these lecture notes, we describe different types of stochastic gravitational-wave backgrounds and introduce the method of cross-correlation for extracting the signal from the noise. Interested readers should see e.g., [7, 9, 41] for more details.

1 Motivation

A stochastic background of gravitational radiation is a superposition of gravitational-wave signals that are either too weak or too numerous to individually detect. The individual signals making up the background are thus *unresolvable*, unlike the large signal-to-noise ratio binary black-hole (BBH) and binary neutron-star (BNS) merger signals that have been recently detected by the advanced LIGO and Virgo detectors [2, 3, 51]. But despite the fact that one cannot resolve the individual signals that comprise the background, the detection of a gravitational-wave background (GWB) will provide information about the *statistical* properties (or population properties) of the source.

1.1 Gravitational-wave analogue of the cosmic microwave background

The ultimate goal of GWB searches is to produce the GW analogue of Figure 1, which is a sky map

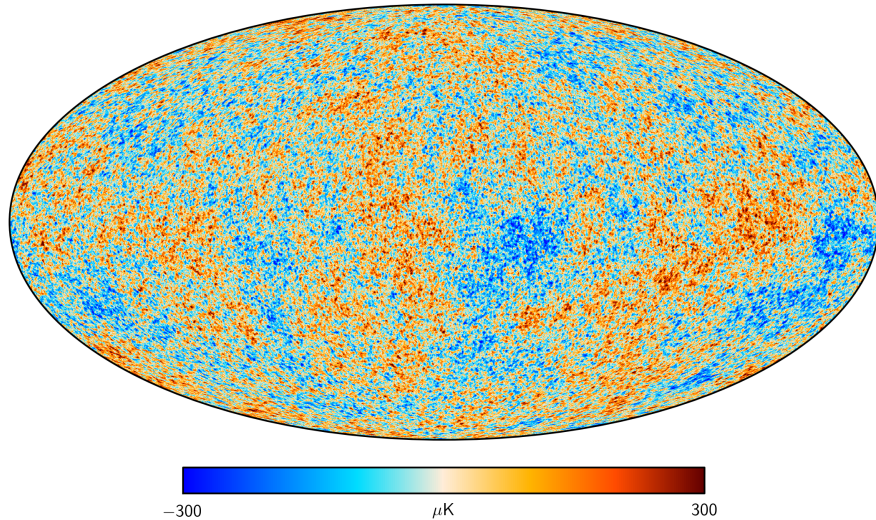


Figure 1: Skymap of $\Delta T/T_0$ for the cosmic microwave background radiation (https://www.cosmos.esa.int/documents/387566/425793/2015_SMICA_CMB/).

of the temperature fluctuations in the cosmic microwave background (CMB) blackbody radiation, $\Delta T/T_0$, relative to the $T_0 = 2.73$ K isotropic component [36, 16]. (The dipole contribution due to our motion with respect to the cosmic rest frame has also been subtracted out.) The CMB is a background of electromagnetic radiation, produced roughly 380,000 yr after the Big Bang [29, 43]. At that time, the universe had a temperature of ~ 3000 K, approximately one thousand times larger than the temperature today, but cool enough for neutral hydrogen atoms to first form and photons to propagate freely. The temperature fluctuations in the CMB radiation tell us about

the density perturbations at the time of last scattering of photons, thus giving us a picture of the “seeds” of large-scale structure formation in the early universe [48, 39]. Given the weakness of the gravitational interaction compared to the electromagnetic force, the GW analogue of Figure 1 would provide information about a much earlier time in the evolution of the universe, a mere fraction of a second after the Big Bang [7, 31] (this is explained in a bit more detail in Section 2.1). Detecting the cosmological GWB is thus a “holy grail” for GW astronomy.

For perspective, Figure 1 was produced by the Planck mission in 2015, 50 years after the CMB radiation was initially detected by Penzias and Wilson [36] in 1965. It took many years and improved experiments (COBE [59], Boomerang [32], WMAP [60], and Planck [61] to name a few) to get to the high-precision measurements that we have today. So it is somewhat sobering to realize that now—in the summer of 2019—we have yet to detect even the isotropic component of the GWB.

1.2 The background of BBH and BNS mergers in the LIGO band

Even though a detailed map of the primordial GWB is likely to be out of reach for many years, there are other sources of GWBs that are much more immediately accessible to us. For example, as mentioned above, the advanced LIGO and Virgo detectors have detected other GW signals from several individual BBH and BNS mergers [51]. These were very strong signals, having matched-filter signal-to-noise ratios (SNR) $\gtrsim 10$, and false alarm probabilities $< 2 \times 10^{-7}$, corresponding to 5-sigma “gold-plated” events. Similar large-SNR detections are expected during the observing run O3, which started on 1 April 2019. But we also expect that there are many more signals, corresponding to more distant mergers or smaller mass systems, which are individually undetectable (i.e., *subthreshold* events). This weaker background of gravitational radiation is nonetheless detectable as a combined/aggregate signal via the common influence of the component GWs on multiple detectors [1, 4].

To get an idea of the statistical properties of this background signal, we can estimate the total rate of stellar-mass BBH mergers throughout the universe by using the local rate estimate from these first detections, $9\text{--}240 \text{ Gpc}^{-3} \text{ yr}^{-1}$ [50]. This leads to a prediction for the total rate of BBH mergers between ~ 1 per minute to a few per hour. (You are asked in Exercise A.1 to verify these predictions.)¹ Since the duration of BBH merger signals in band is ~ 1 s, which is much smaller than the average duration between successive mergers, the combined signal will consist of discrete bursts of radiation separated by periods of silence (i.e., it will be *popcorn-like*). We can perform similar calculations for BNS mergers. The predicted total rate for such events is roughly one event every 15 s, while the duration of a BNS signal in band is roughly 100 s. Thus, the BNS merger signals overlap in time leading to a continuous (or *confusion-limited*) background. Figure 2 is a plot of the expected time-domain signal corresponding to the rate estimates mentioned above.

The combined signal from BBH and BNS mergers is potentially detectable with advanced LIGO and Virgo, shortly after reaching design sensitivity [4]. Although the signal-to-noise ratios for the individual events are small, the combined signal-to-noise ratio of the correlated data summed over all events grows like the square-root of the observation time, reaching a detectable level of 3σ after roughly 40 months of observation (Figure 3). This estimate of time to detection is based on the standard cross-correlation search (Section 4), which assumes a Gaussian-stationary background. But there is a new method [47], recently proposed by Smith and Thrane, which can potentially reduce the time to detection by several orders of magnitude (factor of ~ 1000), meaning that the

¹A more complete description of this and all other exercises are given in Appendix A. The number next to “Exercise” is a link that brings you to the detailed exercise in Appendix A.

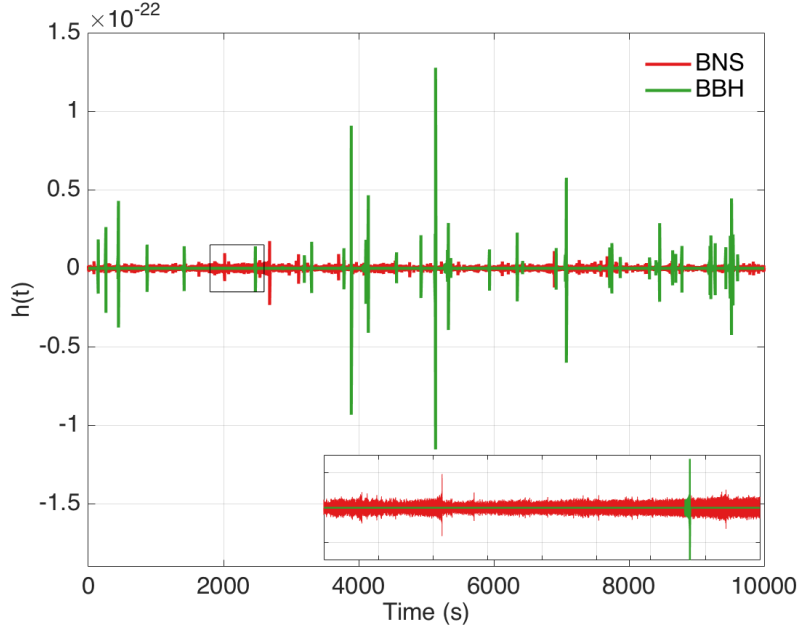


Figure 2: Simulated time-domain signal for the predicted BBH and BNS backgrounds. (Figure taken from [4].)

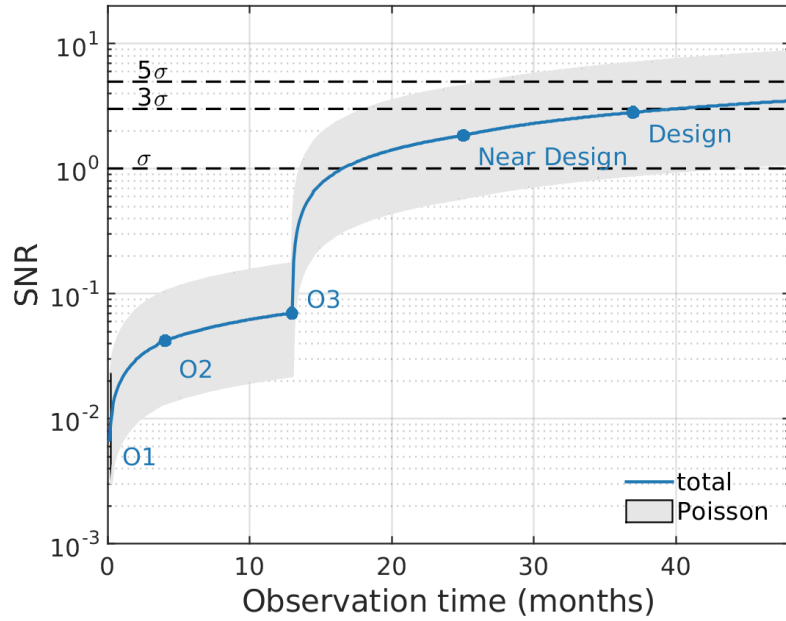


Figure 3: Expected signal-to-noise ratio as a function of observation time for the standard cross-correlation search using the advanced LIGO and Virgo detectors. The points labeled O1, O2, etc., indicate the start of advanced LIGO's first observation run, second observation run, etc. (Figure taken from [4].)

background would be detectable after only a few days of operation. We will describe this method in more detail in Section 9.

2 Different types of stochastic backgrounds

2.1 Different sources

The combined signal from stellar-mass BBH and BNS mergers throughout the universe is just one way of producing a GWB. Due to the relatively small masses of stellar-mass BHs and NSs, the signal is at the high-frequency end of the spectrum (~ 10 Hz to a few kHz), which is the sensitive band for the current generation of km-scale ground-based laser interferometers like LIGO and Virgo. Heavier-mass systems, which produce lower-frequency gravitational waves, are also expected to give rise to GWBs that are potentially detectable with other existing or proposed detectors. Figure 4 is a plot of the GW spectrum, with frequencies ranging from a few kHz (for ground-based detectors) to 10^{-17} Hz (corresponding to a period equal to the age of the universe), together with potential sources of GWBs and relevant detectors.

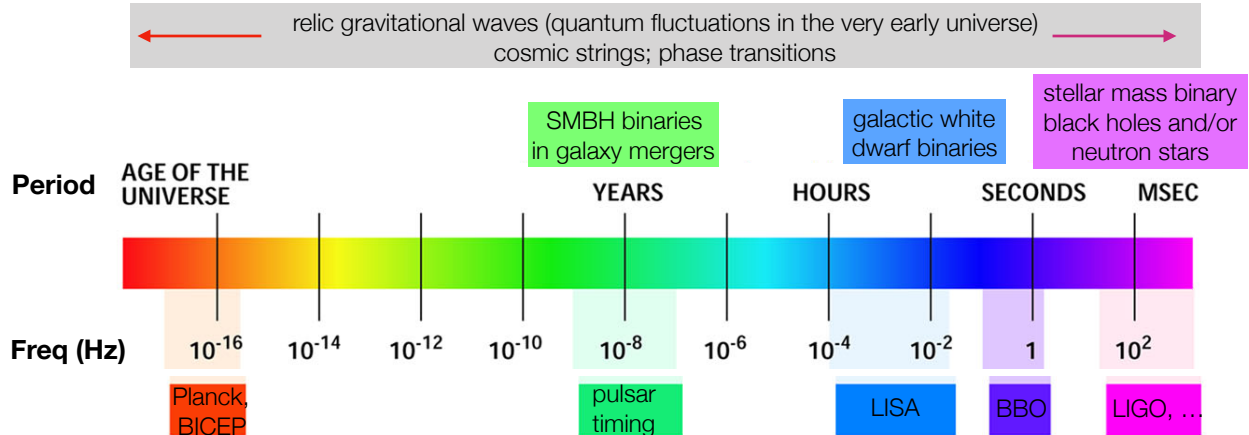


Figure 4: Detectors and potential sources of GWBs across the GW spectrum. Note that the GWB signal from cosmic strings and phase transitions stretch across a broad range of frequencies, and peak at basically any frequency depending on the parameters that define the string network and the energy scale where the phase transition occurs. Also, the primordial background of relic GWs predicted by standard inflation is flat across the whole frequency band shown here. (Figure adapted from [41]).

Of particular note is the combined GW signal produced by compact white-dwarf binaries in the Milky Way, producing a “confusion-limited” GWB in the frequency band $\sim 10^{-4}$ Hz to 10^{-1} Hz [10]. This is a guaranteed signal for the proposed space-based interferometer LISA (expected launch date 2034), which consists of three spacecraft in an equilateral-triangle configuration in orbit around the Sun [62]. Each spacecraft houses two lasers, two telescopes, and two test masses; the arms will be several million km long. The confusion-limited white-dwarf binary signal is expected to be so strong that it will dominate the instrumental noise at low frequencies, forming a GW “foreground” that will have to be contended with when searching for other gravitational sources in the LISA band [6].

At lower frequencies between $\sim 10^{-9}$ Hz and 10^{-7} Hz (corresponding to periods of order decades to years), pulsar timing arrays can be used to search for the GWB produced by the inspiral and merger of supermassive black-holes (SMBHs) in the centers of distant galaxies. A pulsar timing array basically functions as a galactic-scale gravitational-wave detector, with the radio pulses emitted by each pulsar behaving like ‘ticks’ of an extremely stable clock. By carefully monitoring the arrival times of these radio pulses, one can search for a GWB by looking for correlated modulations in the arrival times induced by a passing gravitational wave [44, 15, 24].

In addition to these *astrophysical* GWBs associated with stellar-mass or supermassive BHs and NSs, one also expects backgrounds of *cosmological* origin, produced in the very early universe [22], much before the formation of stars and galaxies. Two examples, indicated in Figure 4, are cosmic strings (line-like topological defects associated with phase transitions in the early universe) and relic gravitational waves (quantum fluctuations in the geometry of space-time, driven to macroscopic scales by a period of rapid expansion—e.g., inflation—a mere $\sim 10^{-32}$ s after the Big Bang); see, e.g., [7, 31] for a discussion of these sources. This relic background is potentially detectable by its effect on the polarization of the CMB radiation [45]. This signal has been searched for by CMB experiments such as Planck and BICEP [55], and is a core target of many proposed future experiments, such as PIXIE [28] and LiteBIRD [56].

2.2 Different signal properties

Not surprisingly, different sources of a GWB give rise, in general, to different properties of the observed signal. These differences are what will allow us to infer the source of the background from the measured signal.

(i) Stochastic backgrounds can differ from one another in terms of the angular distribution of GW power on the sky. Cosmologically-generated backgrounds, like those from cosmic strings or relic GWs, are expected to be *statistically isotropic*, qualitatively similar to the CMB (Figure 1). The GW power in these backgrounds is *anisotropic*, following the spatial distribution of the particular sources that produced it, but has no preferred direction when averaged over different realizations of the sources. Different statistically isotropic backgrounds will be characterized by different angular power spectra, C_l as a function of multipole moment l , where [43]

$$C(\theta) = \sum_{l=0}^{\infty} \frac{2l+1}{4\pi} C_l P_l(\cos \theta), \quad (2.1)$$

is the angular correlation between the GW power coming from two directions \hat{n} and \hat{n}' separated by angle θ . If all of the C_l 's except the monopole, C_0 , are equal to zero, then the GWB is said to be “exactly” isotropic. Exact isotropy is the simplest mathematical model for stochastic backgrounds, and will be discussed further in Section 3.2.

Statistically isotropic backgrounds are to be contrasted with *statistically anisotropic* backgrounds, whose distribution of power on the sky has preferred directions, even when averaged over different realizations of the sources that produce it. For example, the “confusion-limited” foreground that LISA will see from the population of close white-dwarf binaries in the Milky Way will have its GW power concentrated in the direction of the Milky Way. Figure 5 shows simulated skymaps for a statistically isotropic background (left panel) and a statistically anisotropic background (right panel). The anisotropic background in that figure follows the galactic plane in equatorial coordinates.

(ii) Stochastic backgrounds can also differ from one another in temporal distribution and amplitude. We have already seen examples of this in Figure 2, for the expected backgrounds from

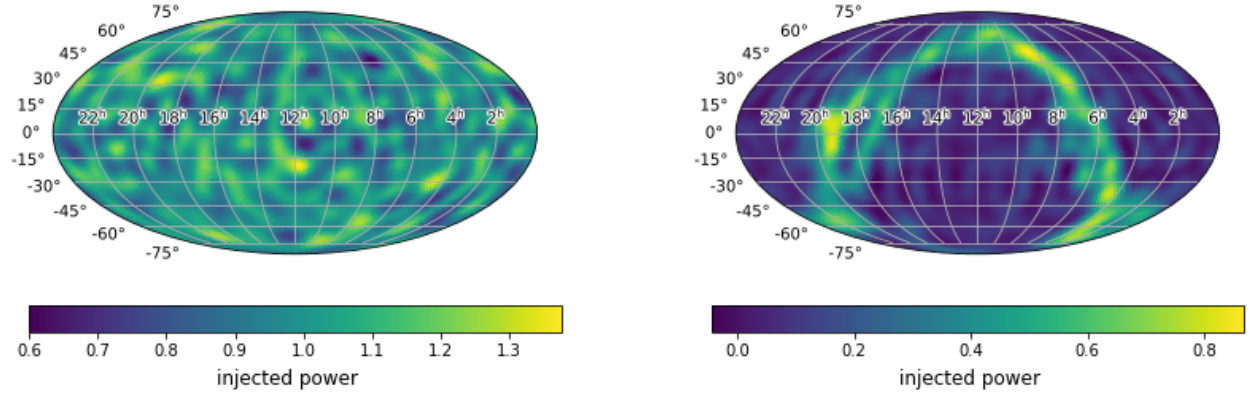


Figure 5: Simulated sky maps of GW power for a statistically isotropic background (left panel) and an anisotropic background (right panel).

stellar-mass BBH mergers and BNS mergers throughout the universe (a LIGO source). As mentioned earlier, the rate estimates and durations of these individual merger signals are such that the BBH background is expected to be popcorn-like (consisting of non-overlapping mergers), while that for the BNS background is expected to be stationary and confusion-limited (consisting of several overlapping BNS mergers at any instant of time). Another example of non-trivial temporal dependence is the confusion-limited signal from close white-dwarf binaries in the Milky Way (a LISA source). This is an amplitude-modulated signal with a 6-month period (Figure 6), due to LISA's

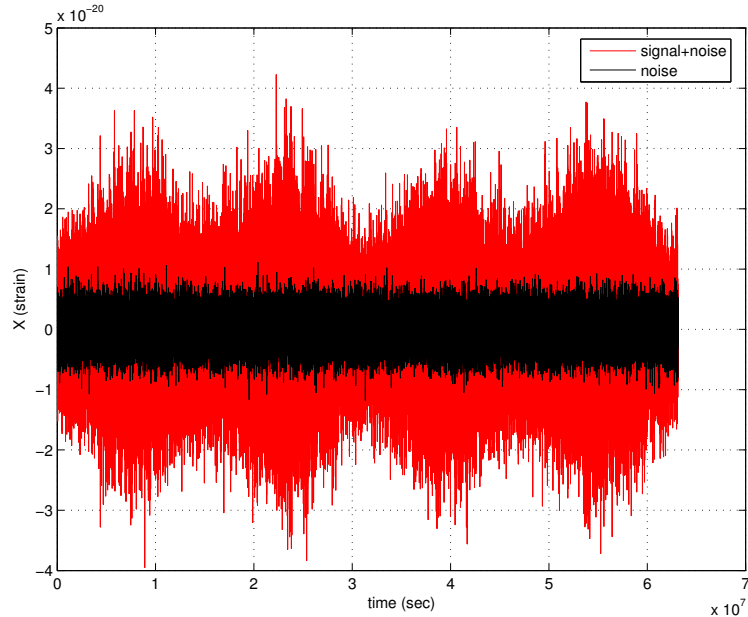


Figure 6: Simulated time-domain output of a particular combination of the LISA data over a 2-year period. The modulation of the signal with a 6-month period is apparent in the data. (Figure taken from [41].)

“cartwheeling” orbital motion around the Sun. (The antenna pattern of LISA will point in the

direction of the Galactic center twice every year.) From the figure, we also see that the expected white-dwarf binary signal will be larger than that of the instrumental noise for LISA, thus constituting an astrophysical *foreground*. This is atypical, however, as most expected GWBs will sit below the instrumental noise (e.g., for advanced LIGO / Virgo, pulsar timing, CMB polarization experiments), requiring observation over long periods of time to confidently detect.

(iii) Stochastic backgrounds can also differ in their power spectra² as shown in Figure 7. Here we plot simulated time-domain data (including the signals for an individual BNS merger and BBH ringdown³), histograms, and power spectra for three different types of GWBs. For these toy-model simulations, we overlapped a sufficient number of individual BNS merger and BBH ringdown signals to produce Gaussian-stationary confusion-limited GWBs (second and third columns). The difference between these backgrounds shows up in their power spectra (fourth column). The power spectra for the BNS merger and BBH ringdown backgrounds have the same shape as those for an individual BNS merger or BBH ringdown, scaled by the total number of sources contributing to the background.

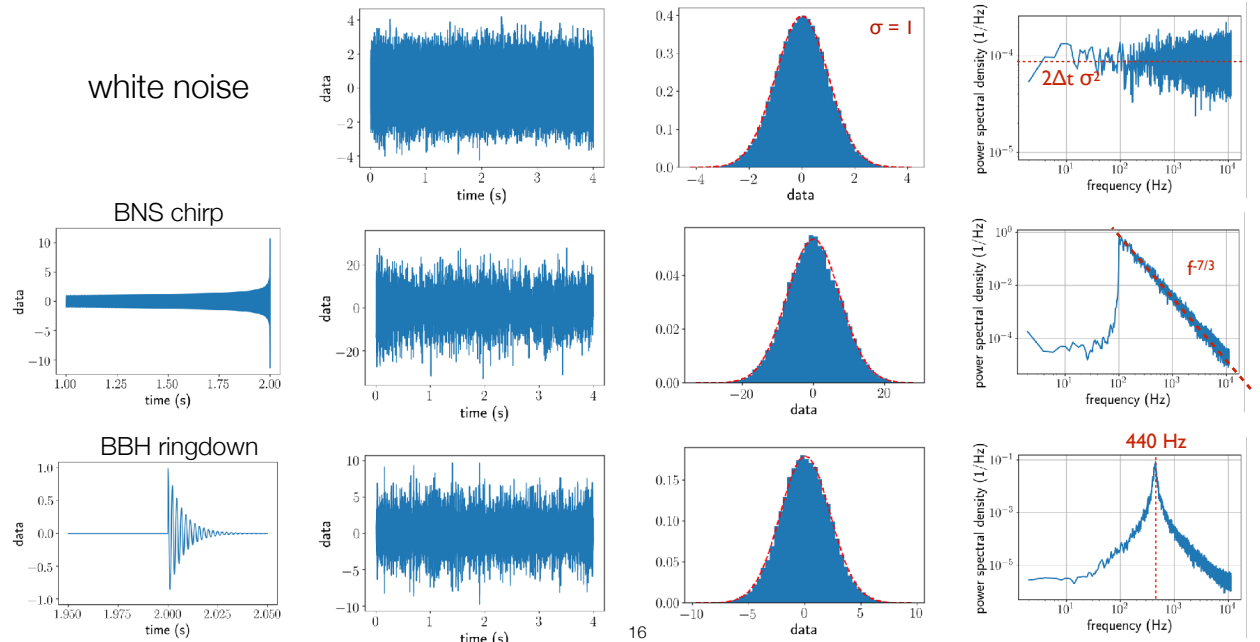


Figure 7: Simulated time-domain data (including the signals for an individual BNS merger and BBH ringdown), histograms, and power spectra for three different types of Gaussian-stationary GWBs.

3 Mathematical characterization of a stochastic background

Since the individual signals comprising a GWB background are either too weak or too numerous to individually detect, the combined signal for the background is for all practical purposes *random*,

²If $x(t)$ is stationary time-domain data, then the power spectrum $P_x(f)$ is defined as the Fourier transform of the correlation function $C(t - t') \equiv \langle x(t)x(t') \rangle$, or, equivalently, $\langle \tilde{x}(f)\tilde{x}^*(f') \rangle = \frac{1}{2}P_x(f)\delta(f - f')$, where $\tilde{x}(f)$ is the Fourier transform of $x(t)$. The factor of 1/2 is needed for a *one-sided* power spectrum; see also (4.15).

³Our toy-model simulation for BBH ringdown is simply a damped sinusoid with frequency 440 Hz. It has the correct qualitative behavior for a BBH ringdown, but is not meant to be astrophysically realistic.

similar to noise in a single detector. Hence, we need to describe the GWB *statistically*, in terms of moments (i.e., ensemble averages) of the metric perturbations describing the GWB.

3.1 Plane-wave expansion

Recall that gravitational waves are time-varying perturbations to the geometry of space-time, which propagate away from the source at the speed of light [34, 23]. In transverse-traceless coordinates $(t, \vec{x}) \equiv (t, x^a)$, where $a = 1, 2, 3$, the metric perturbations corresponding to a plane wave (propagating in direction $\hat{k} \equiv -\hat{n}$) have two degrees of freedom, corresponding to the amplitudes of the plus (+) and cross (\times) polarizations of the gravitational wave (Figure 8). The metric perturbation

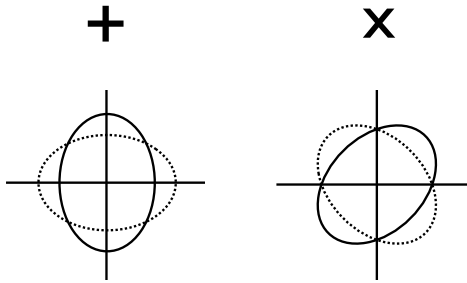


Figure 8: The two orthogonal polarizations of a gravitational wave. A circular ring of test particles in the plane orthogonal to the direction of propagation of the wave are alternately deformed into ellipses, as space is “squeezed” and “stretched” by the passing of the wave.

for the most general GWB can thus be written as a superposition of such waves:

$$h_{ab}(t, \vec{x}) = \int_{-\infty}^{\infty} df \int d^2\Omega_{\hat{k}} \sum_{A=+, \times} h_A(f, \hat{k}) e_{ab}^A(\hat{k}) e^{i2\pi f(t - \hat{k} \cdot \vec{x}/c)}, \quad (3.1)$$

where f denotes the frequency of the component waves, \hat{k} their direction of propagation, and $A = +, \times$ their polarization. (The direction to a particular GW source is given by $\hat{n} = -\hat{k}$.) The quantities $e_{ab}^A(\hat{k})$ are polarization tensors, given by

$$\begin{aligned} e_{ab}^+(\hat{k}) &= \hat{l}_a \hat{l}_b - \hat{m}_a \hat{m}_b, \\ e_{ab}^\times(\hat{k}) &= \hat{l}_a \hat{m}_b + \hat{m}_a \hat{l}_b, \end{aligned} \quad (3.2)$$

where \hat{l}, \hat{m} are any two orthogonal unit vectors in the plane orthogonal to \hat{k} . Typically, for stochastic background analyses, we take \hat{l}, \hat{m} to be proportional to the standard angular unit vectors tangent to the sphere, so that $\{\hat{k}, \hat{l}, \hat{m}\}$ is a right-handed system (Figure 9):

$$\begin{aligned} \hat{k} &= -\sin \theta \cos \phi \hat{x} - \sin \theta \sin \phi \hat{y} - \cos \theta \hat{z} = -\hat{r}, \\ \hat{l} &= +\sin \phi \hat{x} - \cos \phi \hat{y} = -\hat{\phi}, \\ \hat{m} &= -\cos \theta \cos \phi \hat{x} - \cos \theta \sin \phi \hat{y} + \sin \theta \hat{z} = -\hat{\theta}. \end{aligned} \quad (3.3)$$

For analyzing non-stochastic GW sources that have a symmetry axis (e.g., the angular momentum vector for binary inspiral), one takes \hat{l} and \hat{m} to be rotated relative to $-\hat{\phi}$ and $-\hat{\theta}$, where the rotation angle is the *polarization angle* of the source.

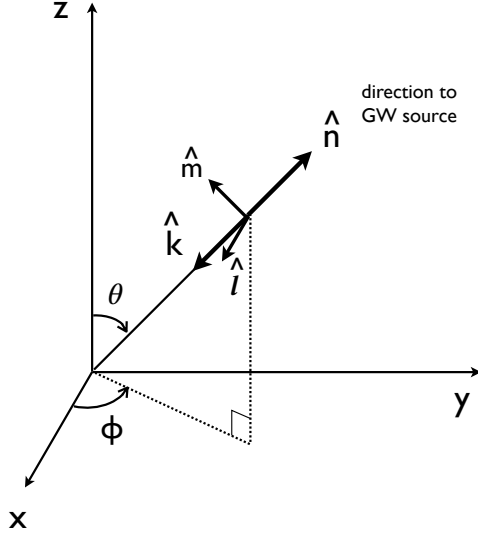


Figure 9: Coordinate system and unit vectors used in the plane-wave expansion of a GWB.

3.2 Ensemble averages

The quantities $h_A(f, \hat{k})$ are the Fourier coefficients of the plane wave expansion. Since the metric perturbations for a stochastic background are random variables, so too are the Fourier coefficients. The probability distributions of the Fourier coefficients thus define the statistical properties of the background.

Without loss of generality, we can assume that the expected value of the Fourier coefficients is zero,

$$\langle h_A(f, \hat{k}) \rangle = 0, \quad (3.4)$$

where angle brackets denote *ensemble average* over different realizations of the background. (The different realizations could be thought of as the different backgrounds observed by different spatially-located observers in a homogeneous and isotropic universe.) The second-order moments (i.e., quadratic expectation values) specify possible correlations between the Fourier coefficients. For example, if the background is *unpolarized, stationary, and isotropic*, then

$$\langle h_A(f, \hat{k}) h_{A'}^*(f', \hat{k}') \rangle = \frac{1}{16\pi} S_h(f) \delta(f - f') \delta_{AA'} \delta^2(\hat{k}, \hat{k}'), \quad (3.5)$$

where $S_h(f)$ is the *strain power spectral density* of the background, having units of strain² Hz⁻¹. The fact that the RHS is proportional to $\delta(f - f')$ is a consequence of the assumption of *stationarity*—i.e., that there is no preferred origin of time. That the RHS depends on the polarization indices only via $\delta_{AA'}$ is a consequence of the background being unpolarized—i.e., that the + and \times polarization components are statistically equivalent and uncorrelated with one another. Similarly, the dependence on GW propagation directions only via $\delta^2(\hat{k}, \hat{k}')$ is a consequence of exact isotropy—i.e., that the power in the GWB has no preferred direction, and that the GWs propagating in different directions have uncorrelated phases.

If we drop the last assumption, allowing the background to be either *anisotropic* or *statistically isotropic*, then the quadratic expectation values become

$$\langle h_A(f, \hat{k}) h_{A'}^*(f', \hat{k}') \rangle = \frac{1}{4} \mathcal{P}(f, \hat{k}) \delta(f - f') \delta_{AA'} \delta^2(\hat{k}, \hat{k}'), \quad (3.6)$$

where

$$S_h(f) = \int d^2\Omega_{\hat{k}} \mathcal{P}(f, \hat{k}). \quad (3.7)$$

Here $\mathcal{P}(f, \hat{k})$ is the strain power spectral density per unit solid angle, with units strain² Hz⁻¹ sr⁻¹. For statistically isotropic backgrounds, the angular power spectrum is given by the coefficients C_l of a Legendre series expansion (2.1) of the two-point function $C(\theta) \equiv \langle \mathcal{P}(f, \hat{k}) \mathcal{P}(f, \hat{k}') \rangle_{\text{sky avg}}$, for all \hat{k}, \hat{k}' having $\cos \theta = \hat{k} \cdot \hat{k}'$.

For *Gaussian* backgrounds, all cubic and higher-order moments are either identically zero or can be written in terms of the second-order moments. Thus, the quadratic expectation values of the Fourier coefficients completely characterize the statistical properties of a Gaussian-distributed background.

3.3 Energy density spectrum in gravitational waves

As mentioned above, $S_h(f)$ is the strain power spectral density of the GWB. It can be related to the (normalized) *energy density spectrum*

$$\Omega_{\text{gw}}(f) \equiv \frac{1}{\rho_c} \frac{d\rho_{\text{gw}}}{d\ln f} = \frac{f}{\rho_c} \frac{d\rho_{\text{gw}}}{df}, \quad (3.8)$$

where $d\rho_{\text{gw}}$ is the energy density in gravitational waves contained in the frequency interval f to $f + df$, and $\rho_c \equiv 3H_0^2 c^2 / 8\pi G$ is the *critical* energy density (that needed to just close the universe today). The result is [9]

$$S_h(f) = \frac{3H_0^2}{2\pi^2} \frac{\Omega_{\text{gw}}(f)}{f^3}, \quad (3.9)$$

which makes use of the relation

$$\rho_{\text{gw}} = \frac{c^2}{32\pi G} \langle \dot{h}_{ab}(t, \vec{x}) \dot{h}^{ab}(t, \vec{x}) \rangle, \quad (3.10)$$

which gives the energy density in gravitational waves in terms of the quadratic expectation values of the metric perturbations. You are asked in Exercise A.2 to derive (3.9); to do so, you will also need to use the plane-wave expansion (3.1) and the quadratic expectation values (3.5) or (3.6).

In addition to $S_h(f)$ and $\Omega_{\text{gw}}(f)$, one sometimes describes the strength of a GWB in terms of the (dimensionless) *characteristic strain* $h_c(f)$ defined by

$$h_c(f) = \sqrt{f S_h(f)}. \quad (3.11)$$

For backgrounds described by a power-law dependence on frequency,⁴

$$h_c(f) = A_\alpha \left(\frac{f}{f_{\text{ref}}} \right)^\alpha \Leftrightarrow \Omega_{\text{gw}}(f) = \Omega_\beta \left(\frac{f}{f_{\text{ref}}} \right)^\beta, \quad (3.12)$$

where α and β are spectral indices, and A_α and Ω_β are the amplitudes of the characteristic strain and energy density spectrum, respectively, at some reference frequency $f = f_{\text{ref}}$. Using the above definitions and relationships between $\Omega_{\text{gw}}(f)$, $S_h(f)$, and $h_c(f)$, we have

$$\Omega_\beta = \frac{2\pi^2}{3H_0^2} f_{\text{ref}}^2 A_\alpha^2, \quad \beta = 2\alpha + 2. \quad (3.13)$$

⁴There is no sum over α or β in the following expressions.

For standard inflationary backgrounds, $\Omega_{\text{gw}}(f) = \text{const}$, for which $\beta = 0$ and $\alpha = -1$. For GWBs associated with binary inspiral, $\Omega_{\text{gw}}(f) \propto f^{2/3}$ (as we shall show below), for which $\beta = 2/3$ and $\alpha = -2/3$. This last dependence is valid for both compact binary coalescences consisting of NSs and/or stellar-mass BHs (relevant for advanced LIGO, Virgo, etc.), and also for SMBH binaries (relevant for pulsar timing searches).

3.4 Calculating $\Omega_{\text{gw}}(f)$ for an astrophysically-generated background

There is a relatively simple formula for calculating the energy density spectrum $\Omega_{\text{gw}}(f)$ produced by a collection of discrete astrophysical GW sources distributed throughout the universe [38]:

$$\Omega_{\text{gw}}(f) = \frac{1}{\rho_c} \int_0^\infty dz n(z) \frac{1}{1+z} \left(f_s \frac{dE_{\text{gw}}}{df_s} \right) \Big|_{f_s=f(1+z)} . \quad (3.14)$$

We will call this the “Phinney formula”, since it was first written down by E.S. Phinney in an unpublished paper in 2001. For this expression, one needs only the comoving number density of sources $n(z)$ as a function of the cosmological redshift z , and the energy spectrum of an individual source dE_{gw}/df_s as measured in its rest frame. The source frame frequency f_s is related to the observed (present-day) frequency f via $f_s = f(1+z)$. The factor of $1/(1+z)$ in the integrand is needed to redshift the energy measured in the source frame to that measured today. Note that the right-hand side of (3.14) is just the right-hand side of (3.8) expanded in terms of its contribution from individual sources.

The above relationship can also be written in terms of the comoving rate density $R(z)$, which is related to the comoving number density $n(z)$ via

$$n(z) dz = R(z) |dt|_{t=t(z)} . \quad (3.15)$$

The final result is

$$\Omega_{\text{gw}}(f) = \frac{f}{\rho_c H_0} \int_0^\infty dz R(z) \frac{1}{(1+z)E(z)} \left(\frac{dE_{\text{gw}}}{df_s} \right) \Big|_{f_s=f(1+z)} , \quad (3.16)$$

where

$$E(z) \equiv \sqrt{\Omega_m(1+z)^3 + \Omega_\Lambda} \quad (3.17)$$

is a cosmological factor that arises when evaluating dt/dz [43]. Ω_m and Ω_Λ are the fractional energy densities for matter (ordinary baryonic matter plus dark matter) and dark energy, with numerical values roughly equal to 0.30 and 0.70, respectively. Exercise A.3 asks you to prove this “rate-version” of the Phinney formula, filling in some of the cosmology-related details.

3.4.1 Example: $\Omega_{\text{gw}}(f)$ for binary inspiral

To illustrate the Phinney formula in action, we will verify the $\Omega_{\text{gw}}(f) \propto f^{2/3}$ power-law dependence for binary inspiral, which we stated without proof at the end of Section 3.3. Since we are interested here only in the frequency dependence of $\Omega_{\text{gw}}(f)$, we just need to calculate the energy spectrum dE_{gw}/df_s for a single binary system.

So let us consider two masses, m_1 and m_2 , in circular orbits around their common center of mass (Figure 10). We make the standard definitions

$$r \equiv r_1 + r_2 , \quad M \equiv m_1 + m_2 , \quad \mu \equiv \frac{m_1 m_2}{m_1 + m_2} \quad (3.18)$$

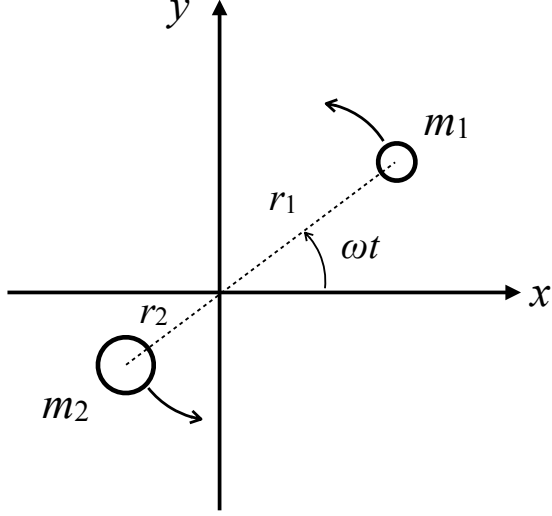


Figure 10: Two masses m_1, m_2 in orbit around their common of mass.

of the *relative separation*, *total mass*, and *reduced mass* of the system. In terms of these quantities, Kepler's third law and the total orbital energy of the system can be written as

$$\omega^2 r^3 = GM, \quad E_{\text{orb}} = -\frac{GM\mu}{2r}, \quad (3.19)$$

where $\omega \equiv 2\pi f_{\text{orb}}$ is the orbital angular frequency. The power emitted in GWs comes from the orbital energy

$$\frac{dE_{\text{gw}}}{dt} = -\frac{dE_{\text{orb}}}{dt}, \quad (3.20)$$

which implies that the energy spectrum is given by

$$\frac{dE_{\text{gw}}}{df_s} = \frac{dt}{df_s} \frac{dE_{\text{gw}}}{dt} = -\frac{dt}{df_s} \frac{dE_{\text{orb}}}{dt}. \quad (3.21)$$

It is now a relatively simple matter to evaluate the RHS of the last expression, using Kepler's law to replace all occurrences of r and \dot{r} with expressions involving ω and $\dot{\omega}$. The final result is

$$\frac{dE_{\text{gw}}}{df_s} \sim \mathcal{M}_c^{5/3} f_s^{-1/3}, \quad \mathcal{M}_c^{5/3} \equiv M^{2/3} \mu, \quad (3.22)$$

where \mathcal{M}_c is the *chirp mass* of the system, and where we have ignored all numerical factors. Note that we also replaced the orbital angular frequency ω by the GW frequency $f_s = 2f_{\text{orb}}$, with the factor of 2 arising for quadrupolar radiation in general relativity.⁵ Returning now to (3.16), we substitute $f_s = (1+z)f$ and multiply by the factor of f outside the integral to get $\Omega_{\text{gw}}(f) \propto f^{2/3}$ as claimed.

4 Correlation methods

As discussed above, a stochastic background of GWs is described by a *random* signal, which looks like noise in a single detector. As such, standard search techniques like *matched filtering* [67, 25],

⁵For elliptical orbits, one should average the radiated power, etc., over a period of the orbit. There will also be contributions to the gravitational radiation from harmonics other than just the quadrupole [37].

which correlate the data against known, deterministic waveforms (e.g., BBH chirps) won't work when trying to detect a GWB. Instead, we have to consider other possibilities:

(i) One possibility is to know the noise sources in our GW detector well enough (in both amplitude and spectral shape) that we can attribute any unexpected excess “noise” to a GWB. This was basically how Penzias and Wilson initially detected the CMB; they saw an excess noise temperature of $\sim 3.5^\circ$ K in their radio antenna that they could not attribute to any other noise source [36]. This is also what one hopes to do with LISA, because the time-delay interferometry (TDI) [17] data combinations that one uses to remove the laser frequency noise are orthogonal to one another [40]. Thus, one cannot cross-correlate these data streams to look for a GWB. Instead, one must properly model the instrumental noise and astrophysical foreground (galactic WD binaries) in order to have a chance to detect a cosmological GWB. Studies by Adams and Cornish [5, 6] have shown that you can separate the detector noise, astrophysical foreground, and cosmological background using differences in their spectral shapes and the modulation of the astrophysical background due to LISA's motion around the Sun (Figure 6).

(ii) Another possibility is to use data from multiple detectors. Then we can look for evidence of a common disturbance in the multiple data streams that is consistent with each detector's response to GWs.

Currently, (i) is not an option for ground-based interferometers since, even though the individual noise sources are understood pretty well, their amplitude is not known precisely enough to attribute any observed excess power to GWs. One would need a really loud GWB relative to the detector noise in order detect it in a way similar to Penzias and Wilson's detection of the CMB. But (ii) is an option as LIGO consists of two detectors, one in Hanford, WA, the other in Livingston, LA [65]. Virgo [66], in Italy, provides a third detector, and soon we will have two more large-scale interferometers: one in Japan, called Kagra [58], and the other in India, called IndIGO [64]. Cross-correlating data from multiple detectors works for detecting a GWB since, even though the signal is random, it is the *same* signal in the different detectors (modulo the physical separation and relative orientation of the detectors). In effect, the random output of one detector is used as a template for the data in another detector. As we shall see below, the signal-to-noise ratio of the cross-correlation grows like the square-root of the observation time. Thus, although the GWB might be weak relative to the noise, it can still be extracted from a cross-correlation measurement if it is observed for a long enough period of time.

4.1 Basic idea

To illustrate the basic idea behind cross-correlation, we will consider first the simplest possible scenario—i.e, a single sample of data from two colocated and coaligned detectors:

$$\begin{aligned} d_1 &= h + n_1, \\ d_2 &= h + n_2. \end{aligned} \tag{4.1}$$

Here h denotes the common GW signal component, and n_1, n_2 denote the corresponding instrumental noise components. Cross-correlating the data for this case amounts to simply taking the product of the two data samples, $\hat{C}_{12} \equiv d_1 d_2$. The expected value of the cross-correlation is

$$\langle \hat{C}_{12} \rangle = \langle d_1 d_2 \rangle = \langle h^2 \rangle + \cancel{\langle hn_2 \rangle}^0 + \cancel{\langle n_1 h \rangle}^0 + \langle n_1 n_2 \rangle, \tag{4.2}$$

where $\langle hn_2 \rangle = 0 = \langle n_1 h \rangle$, since the GW signal and instrumental noise are not correlated with one another. If we further assume that the noise in the two detectors is *uncorrelated* (which is typically

a valid assumption if the detectors are widely separated⁶), then $\langle n_1 n_2 \rangle = 0$, leaving

$$\langle \hat{C}_{12} \rangle = \langle h^2 \rangle \equiv S_h , \quad (4.3)$$

which is just the variance (i.e., power) in the GW signal.

4.2 Extension to multiple data samples

The above analysis can be easily extended to the case of multiple samples:

$$\begin{aligned} d_{1i} &= h_i + n_{1i} , \\ d_{2i} &= h_i + n_{2i} , \end{aligned} \quad (4.4)$$

where $i = 1, 2, \dots, N$. As before, we will assume that the two detectors are coincident and coaligned, and that the noise in the two detectors are uncorrelated with the GW signal and with one another

$$\langle n_{1i} h_j \rangle = 0 , \quad \langle n_{2i} h_j \rangle = 0 , \quad \langle n_{1i} n_{2j} \rangle = 0 . \quad (4.5)$$

We will also assume that the GWB and detector noise are both *white*, which means

$$\langle h_i h_j \rangle = S_h \delta_{ij} , \quad \langle n_{1i} n_{1j} \rangle = S_{n_1} \delta_{ij} , \quad \langle n_{2i} n_{2j} \rangle = S_{n_2} \delta_{ij} , \quad (4.6)$$

where S_h, S_{n_1}, S_{n_2} are the variances (i.e., power) in the GW signal and detector noise, respectively.⁷ For this case, our cross-correlation statistic is the average of the products of the individual data samples

$$\hat{S}_h \equiv \hat{C}_{12} \equiv \frac{1}{N} \sum_{i=1}^N d_{1i} d_{2i} , \quad (4.7)$$

which, as we shall see below, is again an estimator of the power in the GWB (hence the “hat” over the S_h on the LHS of this equation).

Using the above definitions and quadratic expectation values, it is easy to show that

$$\mu \equiv \langle \hat{C}_{12} \rangle = \frac{1}{N} \sum_{i=1}^N \langle d_{1i} d_{2i} \rangle = \frac{1}{N} \sum_{i=1}^N \langle h_i^2 \rangle = S_h . \quad (4.8)$$

Thus, the cross-correlation statistic \hat{C}_{12} is an (unbiased) estimator of the GW power S_h . The variance in this estimator can be calculated via

$$\sigma^2 \equiv \langle \hat{C}_{12}^2 \rangle - \langle \hat{C}_{12} \rangle^2 = \left(\frac{1}{N} \right)^2 \sum_{i=1}^N \sum_{j=1}^N (\langle d_{1i} d_{2i} d_{1j} d_{2j} \rangle - \langle d_{1i} d_{2i} \rangle \langle d_{1j} d_{2j} \rangle) . \quad (4.9)$$

To evaluate the RHS of the above equation, we make use of the identity

$$\langle abcd \rangle = \langle ab \rangle \langle cd \rangle + \langle ac \rangle \langle bd \rangle + \langle ad \rangle \langle bc \rangle , \quad (4.10)$$

⁶Note that global magnetic fields, e.g., Schumann resonances, *can* produce environmental correlations in widely separated detectors [53, 54, 13].

⁷The assumption that both the GWB and detector noise are white is made here just to simplify the analysis. One can use cross-correlation methods for the more general case where the signal and noise power spectral densities are non-trivial functions of frequency; see Section 4.3.

which is valid for zero-mean Gaussian random variables. Using this identity and the quadratic expectation values between the signal and noise, we end up with

$$\sigma^2 = \frac{1}{N}(S_1 S_2 + S_h^2), \quad (4.11)$$

where

$$S_1 \equiv S_{n_1} + S_h, \quad S_2 \equiv S_{n_2} + S_h, \quad (4.12)$$

are the total power in the detector output (consisting of both signal and noise power). Note that the factor of $1/N$ in (4.11) comes from the double sum in (4.9) having non-zero contributions from only the diagonal terms ($i = j$), which are all equal to one another.

Since the power in the GWB is expected to be weak compared to the detector noise, the variance can be approximated as $\sigma^2 \simeq S_1 S_2 / N$, for which the expected signal-to-noise ratio is given by

$$\rho \equiv \frac{\mu}{\sigma} \simeq \frac{S_h}{\sqrt{S_1 S_2 / N}} \simeq \sqrt{N} \frac{S_h}{S_n}, \quad (4.13)$$

where $\sqrt{S_1 S_2} \simeq \sqrt{S_{n_1} S_{n_2}} \equiv S_n$. This result verifies the statement made earlier that the signal-to-noise ratio for a cross-correlation measurement grows like the square-root of the observation time (in this case, the total number of samples).

4.3 Optimal filtering

To handle the case of physically-separated and misaligned detectors, we need to include the non-trivial response of a GW detector to a GWB. We will do this in detail in Sections 6 and 7. Here, it suffices to simply define the *overlap function* (or overlap reduction function), denoted $\Gamma_{12}(f)$, as the transfer function relating the strain power in the GWB, $S_h(f)$, to the cross-correlated signal power in the two detectors [18, 12]:

$$C_{12}(f) \equiv \Gamma_{12}(f) S_h(f). \quad (4.14)$$

In terms of the quadratic expectation values of the GW signal in the two detectors, we have⁸:

$$\langle \tilde{h}_1(f) \tilde{h}_2^*(f') \rangle = \frac{1}{2} \delta(f - f') \Gamma_{12}(f) S_h(f), \quad (4.15)$$

where $\tilde{h}_1(f)$, $\tilde{h}_2(f)$ denote the Fourier transforms of the GW signal components $h_1(t)$, $h_2(t)$ in the two detectors. For comparison, the (auto-correlated) power spectra of the detector noise $P_{n_1}(f)$, $P_{n_2}(f)$ can be written in terms of the noise components $\tilde{n}_1(f)$, $\tilde{n}_2(f)$ via:

$$\begin{aligned} \langle \tilde{n}_1(f) \tilde{n}_1^*(f') \rangle &= \frac{1}{2} \delta(f - f') P_{n_1}(f), \\ \langle \tilde{n}_2(f) \tilde{n}_2^*(f') \rangle &= \frac{1}{2} \delta(f - f') P_{n_2}(f), \end{aligned} \quad (4.16)$$

while the cross-correlated noise is assumed to be zero:

$$\langle \tilde{n}_1(f) \tilde{n}_2^*(f') \rangle = 0. \quad (4.17)$$

⁸The factor of $1/2$ is included on the RHS so that the power spectrum is *one-sided*. In other words, the total cross-correlated power in the GWB is given by the integral of $\Gamma_{12}(f) S_h(f)$ over just the *positive* frequencies. The factor of $\delta(f - f')$ is a consequence of stationarity.

Plots of $\Gamma_{12}(f)$ for the LIGO Hanford-LIGO Livingston interferometer pair and for the LIGO Hanford-Virgo interferometer pair can be found in Section 7.2; other examples of overlap functions are also given in that section.

Given the above definitions, we can now ask the question: “What is the optimal way to correlate data from two physically separated and possibly mis-aligned detectors to search for a GWB?” To answer this question, we start by forming the generic cross-correlation

$$\hat{C}_{12} = \int_{-T/2}^{T/2} dt \int_{-T/2}^{T/2} dt' d_1(t) d_2(t) Q(t, t') , \quad (4.18)$$

where $Q(t, t')$ is an a priori arbitrary filter function and T is the observation time. For stationary data, $Q(t, t')$ should depend only on the difference between the two time arguments, $\Delta t \equiv t - t'$, so that $Q(t, t') \equiv Q(t - t')$. In the Fourier domain, we can then write

$$\hat{C}_{12} \simeq \int_{-\infty}^{\infty} df \int_{-\infty}^{\infty} df' \delta_T(f, f') \tilde{d}_1(f) \tilde{d}_2^*(f') \tilde{Q}^*(f') , \quad (4.19)$$

where $\tilde{Q}(f)$ is the Fourier transform of $Q(\Delta t)$, and $\delta_T(f - f')$ is a finite-time version of the Dirac delta function defined by $\delta_T(f - f') \equiv T \text{sinc}[\pi(f - f')T]$, where $\text{sinc } x \equiv \sin x/x$.

To proceed further we need to define what we mean by *optimal*. A natural criterion in this context is to maximize the expected signal-to-noise ratio of \hat{C}_{12} for a GWB with a fixed spectral shape $H(f)$. (The expected signal-to-noise ratio is defined as in the previous section $\rho \equiv \mu/\sigma$, where $\mu \equiv \langle \hat{C}_{12} \rangle$ and $\sigma^2 \equiv \langle \hat{C}_{12}^2 \rangle - \langle \hat{C}_{12} \rangle^2$.) As you are asked to show in Exercise A.4, this maximization condition determines the form of the filter function $\tilde{Q}(f)$ up to an overall normalization [7, 9]

$$\tilde{Q}(f) \propto \frac{\Gamma_{12}(f) H(f)}{P_1(f) P_2(f)} , \quad (4.20)$$

where $P_1(f)$, $P_2(f)$ are the total power in the two detectors,

$$P_1(f) \equiv P_{n1}(f) + P_h(f) , \quad P_2(f) \equiv P_{n2}(f) + P_h(f) , \quad (4.21)$$

which are approximately equal to $P_{n1}(f)$, $P_{n2}(f)$ under the assumption that the GW signal is weak compared to the detector noise. Note that the numerator of $\tilde{Q}(f)$ is proportional to the expected value of the cross-correlated data in the frequency domain, $\langle \tilde{d}_1(f) \tilde{d}_2^*(f) \rangle$, while the denominator basically de-weights the correlation when the detector noise is large. The dependence of $\tilde{Q}(f)$ on the spectral shape $H(f)$ means that the optimal filter is tuned to a particular GWB.

The overall normalization of the optimal filter $\tilde{Q}(f)$ is not determined by the maximization condition, since a constant multiplicative factor cancels out when calculating the signal-to-noise ratio $\rho = \mu/\sigma$. Typically, we use this freedom in the choice of normalization to set the expected value μ of the cross-correlation equal to the overall amplitude of the background—i.e., $\mu = \Omega_{\text{gw}}(f_{\text{ref}})$. In other words, for this choice of normalization, the measured value of the cross-correlation statistic, \hat{C}_{12} , is a *point estimate* of $\Omega_{\text{gw}}(f_{\text{ref}})$.

5 Optimal filtering applied to some simple examples

We now apply the above correlation methods to analyze some simple examples involving simulated data. (The simulations are solely meant to illustrate how optimal filtering works; the amplitude

and duration of the simulated data are not representative of real interferometer data.⁹⁾ We will consider three different GWBs injected into uncorrelated, white detector noise in two coincident and coaligned detectors: (i) a white GWB, (ii) a confusion-limited BNS background, and (iii) a two-component background, formed from the superposition of the GWBs from (i) and (ii). The simulated time-domain data for the three different cases are shown in Figure 11. Recall that a white GWB has a flat spectrum $H(f) = 1$, while a confusion-limited background produced by BNS inspirals and mergers has spectral shape $H(f) = (f/f_{\text{ref}})^{-7/3}$ (see Figure 7).

5.1 Single-component analyses

We start by applying the single-component optimal-filter analysis of the previous section. For example (i), we find that the measured and injected values of the amplitude of the GWB agree to 3.5%, which is within $1-\sigma$. The corresponding optimally-filtered signal-to-noise ratio is $\rho = 2.9$. For example (ii), the measured and injected values of the amplitude of the GWB agree to 2.7%, which again is within $1-\sigma$. The corresponding optimally-filtered signal-to-noise ratio for this case is $\rho = 12$. Note that even though the overall amplitude of the background is noticeably smaller for the confusion-limited BNS background, the signal-to-noise ratio is considerably larger (12 versus 2.9). This is because the spectrum of the GW signal differs in this case from that of the detector noise, which helps in distinguishing the signal and noise components.

Finally for example (iii), if we filter the data for the two components separately, we overestimate the amplitude of the white GWB component by 48%, which is greater than $1-\sigma$, and overestimate the amplitude of the BNS background by 6.9%, which is within $1-\sigma$. Basically, filtering the data for each GWB component separately typically leads to *overestimates* of the amplitudes of the individual components, but *underestimates* of the error bars. The overestimates arise since the other GWB component is also contributing to the correlated signal.

5.2 Multi-component analysis

To better extract the amplitudes of the individual components for example (iii), we need to go beyond single-component optimal-filtering, and consider a signal model that allows for a superposition of multiple GWB components [35]. So instead of taking the cross-correlation to be a *single number*, \hat{C}_{12} , which is obtained by integrating the contributions from all frequencies, we will keep the frequency-dependence explicit, defining

$$\hat{C}_{12}(f) \equiv \frac{2}{T} \tilde{d}_1(f) \tilde{d}_2^*(f), \quad (5.1)$$

where $\tilde{d}_1(f)$, $\tilde{d}_2(f)$ are the Fourier transforms of the time-domain data $d_1(t)$, $d_2(t)$ from the two detectors. We will treat the values of $\hat{C}_{12}(f)$ for different frequencies f as the ‘data points’ from which to construct a *likelihood function*, which is the probability of the data given the parameters defining the signal and noise models.¹⁰ For this case, the signal model is given by the expected value of the correlated data:

$$\langle \hat{C}_{12}(f) \rangle = \sum_{\alpha} \Gamma_{12}(f) A_{\alpha} H_{\alpha}(f) \equiv \sum_{\alpha} M_{\alpha}(f) A_{\alpha}, \quad (5.2)$$

⁹⁾The simulated data used for these examples can be found at [57]. Access to real GW data is available via the Gravitational-Wave Open Science Center (GWOSC) [63].

¹⁰⁾See Section 8 and John Veitch’s lectures in this Volume for more details regarding likelihood functions and statistical inference.

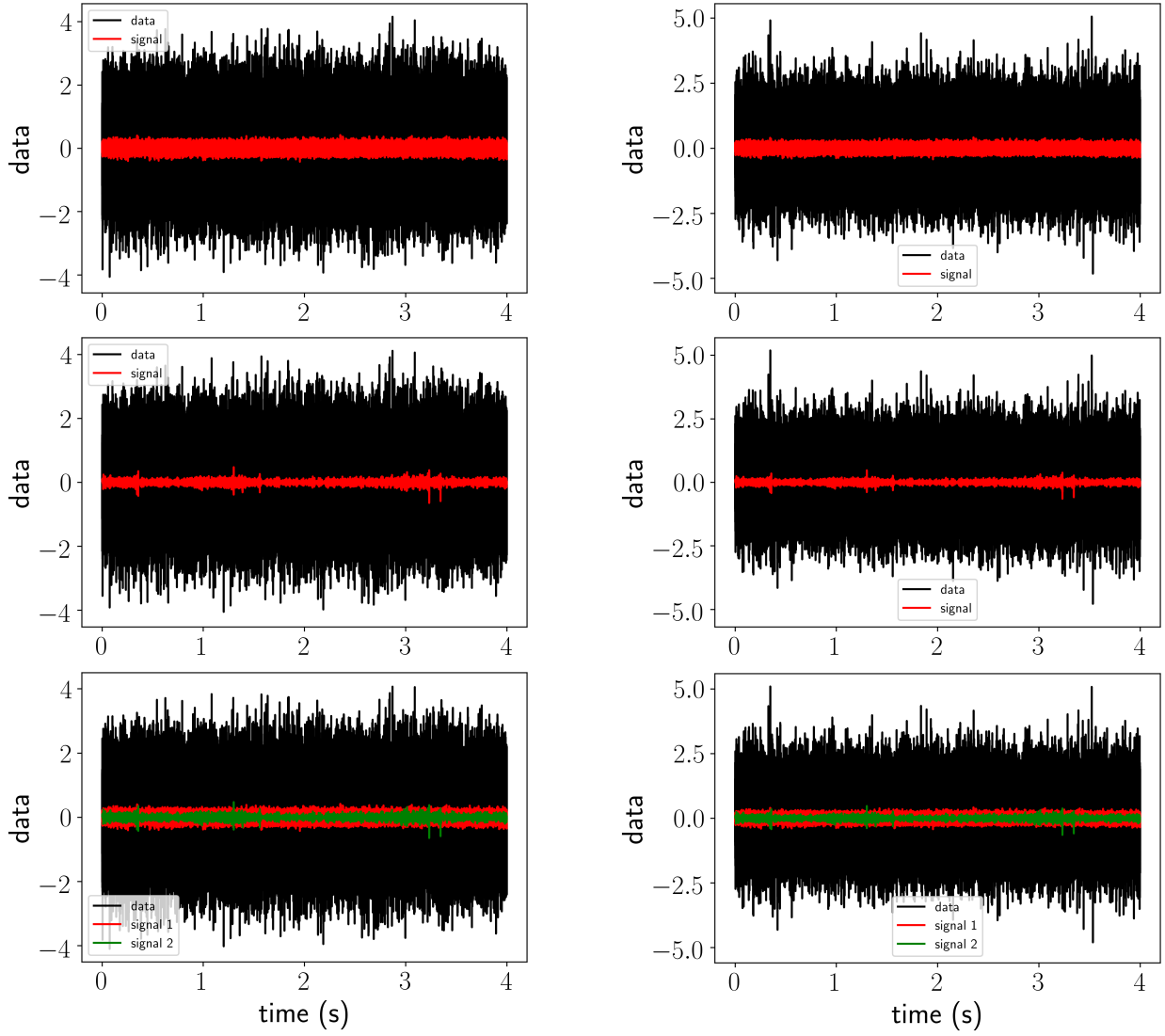


Figure 11: Simulated time-domain data for the three different cases discussed in the main text: (top row) a white GWB in uncorrelated, white detector noise, (middle row) a confusion-limited BNS background in uncorrelated, white detector noise, (bottom row) a two-component background formed from the superposition of the GWBs from the top two rows in uncorrelated, white detector noise. The two columns correspond to data in the two coincident and coaligned detectors. By eye one can see that signal components in the two detectors are identical, but the noise (and hence the data) in the two detectors are different.

where $H_\alpha(f)$ are the different spectral shapes having amplitudes A_α . (Abstractly, we can think of $M_\alpha(f) \equiv \Gamma_{12}(f)H_\alpha(f)$ as a matrix with indices f and α , where f runs over different frequency bins and α runs over different spectral components.) The noise model enters via the covariance matrix of the data:

$$N_{12}(f, f') \equiv \langle \hat{C}_{12}(f)\hat{C}_{12}^*(f') \rangle - \langle \hat{C}_{12}(f) \rangle \langle \hat{C}_{12}^*(f') \rangle \simeq \delta_{ff'} P_1(f)P_2(f), \quad (5.3)$$

which is the product of the noise power spectra in the two detectors in the weak-signal approximation. The likelihood function is then

$$\begin{aligned} p(\hat{C}|A, N) &\propto \exp \left[-\frac{1}{2}(\hat{C} - MA)^\dagger N^{-1}(\hat{C} - MA) \right] \\ &\propto \exp \left[-\frac{1}{2} \int_{-\infty}^{\infty} df \frac{|\hat{C}_{12}(f) - \sum_\alpha M_\alpha(f)A_\alpha|^2}{P_1(f)P_2(f)} \right], \end{aligned} \quad (5.4)$$

which is the probability of the cross-correlated data $\hat{C}_{12}(f)$ given the amplitudes A_α of the GWB spectral components and the noise in the two detectors $N_{12}(f, f')$. The advantage of using an index-free matrix notation, as we did in the first line of the above expression, is that we can use standard linear algebra calculations to find the values of A that maximize the likelihood.

Given the likelihood $p(\hat{C}|A, N)$, we can now obtain estimators of the amplitudes of the GWB components by maximizing it with respect to the A_α . The final result (which you are asked to show in Exercise A.5) is:

$$\hat{A} = F^{-1}X, \quad (5.5)$$

where

$$F \equiv M^\dagger N^{-1} M, \quad X \equiv M^\dagger N^{-1} \hat{C}. \quad (5.6)$$

The quantity F is called the *Fisher information matrix*. In terms of its components,

$$F_{\alpha\beta} = \int_{-\infty}^{\infty} df \frac{H_\alpha(f)\Gamma_{12}^2(f)H_\beta(f)}{P_1(f)P_2(f)}. \quad (5.7)$$

Thus, we see that the Fisher matrix is a noise-weighted inner product of the spectral shapes $H_\alpha(f)$, $H_\beta(f)$ with one another. Provided the spectral shapes are not degenerate (i.e., not proportional to one another), then the Fisher matrix F can be inverted and \hat{A} calculated. Otherwise, some form of regularization is needed to perform the matrix inversion. The inverse of the Fisher matrix, F^{-1} , turns out to equal the covariance matrix of the estimators \hat{A} .

Using the above multi-component formalism, we are now able to extract the amplitude of the white GWB component to 7.3%, corresponding to a signal-to-noise ratio of 1.4, and to extract the amplitude of the BNS background component to 3.8%, corresponding to a signal-to-noise ratio of 6.0. In essence, the *joint* multi-component analysis properly takes into account the *covariance* between the spectral shapes of the two components, allowing for unbiased, minimal variance estimates of the amplitudes A_α .

Part II

Details / Examples

In the second part of these lecture notes, we describe the non-trivial response of a beam detector to gravitational waves, calculate the overlap function between a pair of detectors, and introduce a Bayesian method that can optimally search for the astrophysical background produced by stellar-mass binary BHs throughout the universe.

6 Non-trivial detector response

To understand stochastic background searches on a more quantitative level, we need to describe the non-trivial response of a GW detector to a passing GW. In Section 4.3, we defined the overlap function $\Gamma_{12}(f)$ for a pair of detectors, but we didn't specify how to calculate it, or how its form differs for different GW detectors. In this and the following section, we will develop the tools that we need to do these calculations.

6.1 Beam detectors and different types of detector response

For simplicity, we will restrict our attention to *beam detectors*, which use electromagnetic radiation to monitor the separation of two or more test masses. Laser interferometers (both ground-based and space-based), spacecraft Doppler tracking, and pulsar timing arrays are all examples of beam detectors. (A resonant-bar detector, like that first used by Joseph Weber, is a much different type of detector. Roughly speaking, a resonant bar detector responds like a giant tuning fork to a passing GW, provided the GW has frequencies equal to the resonant frequencies of the bar [34].) The response of a beam detector to a passing GW is the change in the light-travel time $\Delta T(t)$ between the two masses relative to the nominal light-travel time. This is illustrated schematically in Figure 12.

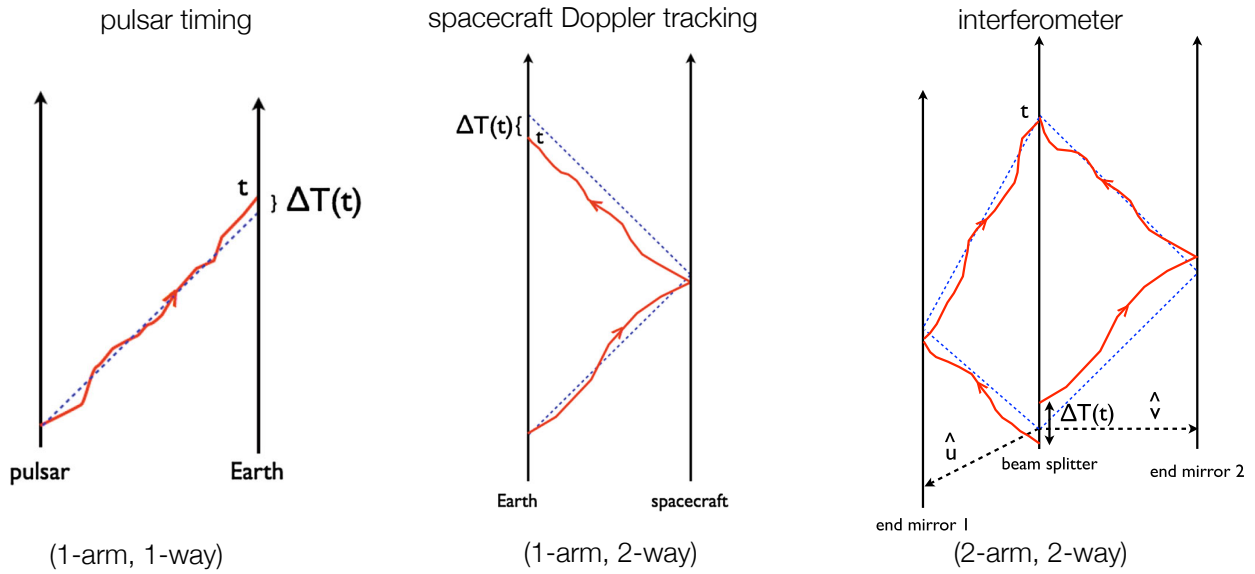


Figure 12: Spacetime diagram showing the response of beam detectors to a passing GW. Left: pulsar timing; middle: spacecraft Doppler tracking; right: interferometer (ground or space-based). A passing GW perturbs the path of the photon (red trajectory) relative to its nominal path in the absence of the wave (blue dotted line), leading to a difference in the expected arrival time of the photon. (Figure adapted from [41].)

In the literature, one might see the detector response written in terms of strain $\Delta L(t)/L$, fractional Doppler frequency $\Delta v(t)/\nu_0$, or phase $\Delta\Phi(t)$, instead of the timing residual $\Delta T(t)$. Despite the apparent differences in the responses, they are all derivable from the change in light

travel time $\Delta T(t)$ via the relations:

$$\begin{aligned}
h(t) &\equiv \Delta T(t) && \text{(pulsar timing)} \\
h(t) &\equiv \frac{\Delta L(t)}{L} = \frac{\Delta T(t)}{T} && \text{(LIGO, Virgo, \dots)} \\
h(t) &\equiv \frac{\Delta\nu(t)}{\nu_0} = \frac{d\Delta T(t)}{dt} && \text{(spacecraft Doppler tracking)} \\
h(t) &\equiv \Delta\Phi(t) = 2\pi\nu_0 \Delta T(t) && \text{(LISA).}
\end{aligned} \tag{6.1}$$

Hence, once we know how to calculate the timing residual response $\Delta T(t)$, we can easily calculate all the other quantities listed above.

6.2 Detector response functions

Gravitational waves are weak. As such, a GW detector acts like a *linear* system,¹¹ converting metric perturbations $h_{ab}(t, \vec{x})$ to the detector output. Mathematically, this is represented by the *convolution* of the metric perturbations with the *response function* of the detector:

$$h(t) = (\mathbf{R} * \mathbf{h})(t, \vec{x}) \equiv \int_{-\infty}^{\infty} d\tau \int d^3y R^{ab}(\tau, \vec{y}) h_{ab}(t - \tau, \vec{x} - \vec{y}). \tag{6.2}$$

Here $h(t)$ is the output of the detector at time t . The vector \vec{x} is the location of detector, and $R^{ab}(\tau, \vec{y})$ is the *impulse response* of the detector. Expanding $h_{ab}(t - \tau, \vec{x} - \vec{y})$ as a sum of plane waves (3.1), and substituting this into the right-hand side of the above expression, we find that the Fourier transform $\tilde{h}(f)$ of $h(t)$ can be written as

$$\tilde{h}(f) = \int d^2\Omega_{\hat{n}} \sum_{A=+, \times} R^A(f, \hat{k}) h_A(f, \hat{k}), \tag{6.3}$$

where

$$R^A(f, \hat{k}) \equiv R^{ab}(f, \hat{k}) e_{ab}^A(\hat{k}) \tag{6.4}$$

and

$$R^{ab}(f, \hat{k}) \equiv e^{-i2\pi f \hat{k} \cdot \vec{x}/c} \int_{-\infty}^{\infty} d\tau \int d^3y R^{ab}(\tau, \vec{y}) e^{-i2\pi f(\tau - \hat{k} \cdot \vec{y}/c)}. \tag{6.5}$$

Note that $R^A(f, \hat{k})$ is the detector response for a plane-wave with frequency f , propagation direction \hat{k} , and polarization A .

6.3 Examples

We now calculate the detector response functions for a couple of examples.

6.3.1 Detector response for a one-arm, one-way detector

For our first example, we will consider the timing response of a one-arm, one-way beam detector, which is relevant for pulsar timing observations. The geometry of the situation is shown in Figure 13. The timing residual response is then given by

$$h(t) \equiv \Delta T(t) = \frac{1}{2c} u^a u^b \int_0^L ds h_{ab}(t(s), \vec{x}(s)), \tag{6.6}$$

¹¹It is a linear system because second and higher-order terms in the metric perturbations can be safely ignored.

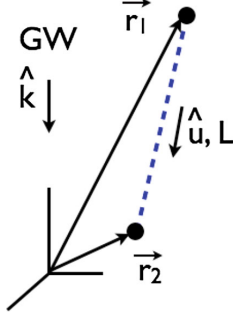


Figure 13: Geometry for a one-arm, one-way beam detector, relevant for a pulsar timing residual measurement. The GW propagates in the \hat{k} direction; the electromagnetic wave (e.g., a radio pulse from a pulsar) propagates in the \hat{u} direction (opposite of the direction to the pulsar, $\hat{p} = -\hat{u}$). (Figure taken from [41].)

where

$$t(s) = (t - L/c) + s/c, \quad \vec{x}(s) = \vec{r}_1 + s\hat{u} \quad (6.7)$$

is a parametric representation of the photon path from the source ($s = 0$) to the detector ($s = L$). Note that we do not need to include any corrections to the straight-line path for the photon given above, as the metric perturbations are already first-order and we can ignore all second and higher-order terms in the calculation.

To do the integral, we first substitute $t(s)$ and $\vec{x}(s)$ for t and \vec{x} in the plane-wave expansion for $h_{ab}(t, \vec{x})$. The s dependence shows up only in the exponential:

$$\begin{aligned} e^{i2\pi f(t(s) - \hat{k} \cdot \vec{x}(s)/c)} &= e^{i2\pi f(t-L/c+s/c - \hat{k} \cdot (\vec{r}_1 + s\hat{u})/c)} \\ &= e^{i2\pi f(t-L/c - \hat{k} \cdot \vec{r}_1/c)} e^{i2\pi f(1 - \hat{k} \cdot \hat{u})s/c}, \end{aligned} \quad (6.8)$$

and the integral over s is easy to do:

$$\int_0^L ds e^{i2\pi f(1 - \hat{k} \cdot \hat{u})s/c} = \frac{c}{i2\pi f} \frac{1}{1 - \hat{k} \cdot \hat{u}} \left[e^{\frac{i2\pi f L}{c}(1 - \hat{k} \cdot \hat{u})} - 1 \right]. \quad (6.9)$$

Then including all the other factors and rearranging terms, you should find (Exercise A.6):

$$R^A(f, \hat{k}) = \frac{1}{i2\pi f} \frac{1}{2} u^a u^b e_{ab}^A(\hat{k}) \frac{1}{1 - \hat{k} \cdot \hat{u}} \left[1 - e^{-\frac{i2\pi f L}{c}(1 - \hat{k} \cdot \hat{u})} \right] e^{-i2\pi f \hat{k} \cdot \vec{r}_2/c}. \quad (6.10)$$

In the context of pulsar timing, the two terms in square brackets are called the *Earth term* and *pulsar term*, respectively. The pulsar term encodes information about the phase of the GW at the location of the pulsar, at the time the radio pulse was emitted. The pulsar term is usually ignored for stochastic background searches, as this term for different pulsars will not be correlated with one other (since the spatial distance between two pulsars, of order kpc, is much greater than the wavelengths of the GWs that pulsar timing arrays are sensitive to, of order 10 light-years).

Both terms are important for LISA data analysis, however, as the wavelengths of the GWs that LISA will be sensitive to are of the same order of magnitude as the lengths of LISA's arms (i.e., the separation between the spacecraft). For this case, one defines a *timing transfer function* for

one-way photon propagation as

$$\begin{aligned}\mathcal{T}_{\hat{u}}(f, \hat{k} \cdot \hat{u}) &\equiv \frac{1}{i2\pi f} \frac{1}{1 - \hat{k} \cdot \hat{u}} \left[1 - e^{-\frac{i2\pi f L}{c}(1 - \hat{k} \cdot \hat{u})} \right] \\ &= \frac{L}{c} e^{-\frac{i\pi f L}{c}(1 - \hat{k} \cdot \hat{u})} \text{sinc} \left(\frac{\pi f L}{c} [1 - \hat{k} \cdot \hat{u}] \right),\end{aligned}\quad (6.11)$$

where $\text{sinc } x \equiv \sin x/x$. Note that for normal incidence (i.e., $\hat{k} \cdot \hat{u} = 0$), the timing transfer function has zeroes when L is equal to an integer number of GW wavelengths $\lambda \equiv c/f$ —i.e., when fL/c equals an integer (Figure 14). This is because a photon’s trajectory undergoes an integer number of cycles of contraction and dilation produced by the GW when $fL/c = 1, 2, \dots$, thereby giving a net zero effect.

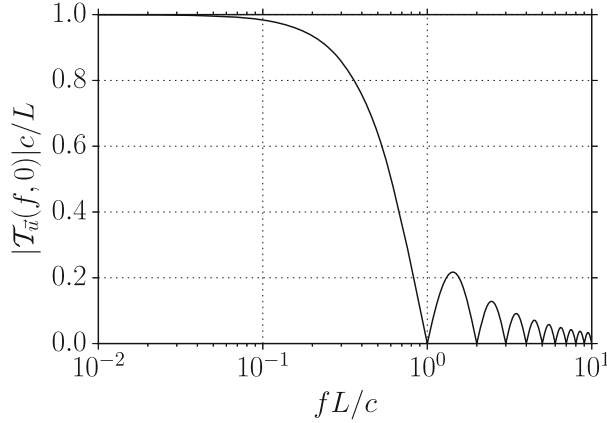


Figure 14: Plot of the absolute value of the timing transfer function $|\mathcal{T}_{\hat{u}}(f, 0)|$ for normal incidence. Note the nulls in the response when L equals an integer number of GW wavelengths $\lambda \equiv c/f$. (Figure taken from [41].)

Returning to (6.10) and its application to pulsar timing analyses, note that the factor $1/(i2\pi f)$ goes away for the Doppler frequency response, $\Delta\nu(t)/\nu_0$, and that the phase term $e^{-i2\pi f \hat{k} \cdot \vec{r}_2/c}$ equals one if we take the \vec{r}_2 to be the origin of coordinates, e.g., at the solar system barycenter. Thus, ignoring the pulsar term, the Doppler frequency response is given simply by

$$F^A(\hat{k}) = \frac{1}{2} \frac{u^a u^b}{1 - \hat{k} \cdot \hat{u}} e_{ab}^A(\hat{k}). \quad (6.12)$$

A plot of the root-summed-squared response (summed over the two polarizations) is shown in Figure 15 for the case $\hat{u} = -\hat{z}$ (or, equivalently, $\hat{p} = \hat{z}$ where $\hat{p} = -\hat{u}$ is the direction to the pulsar). The response is maximum when the GW and radio pulse propagate in the same direction—i.e., when $\hat{k} = \hat{u}$. It is zero when they propagate in opposite directions. These results follow from

$$\begin{aligned}u^a u^b e_{ab}^+(\hat{k}) &= -\sin^2 \theta = -(1 - \cos \theta)(1 + \cos \theta), \\ u^a u^b e_{ab}^\times(\hat{k}) &= 0, \\ 1 - \hat{k} \cdot \hat{u} &= 1 - \cos \theta,\end{aligned}\quad (6.13)$$

for which

$$F^+(\hat{k}) = -\frac{1}{2}(1 + \cos \theta), \quad F^\times(\hat{k}) = 0. \quad (6.14)$$

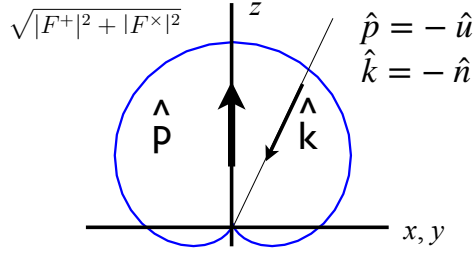


Figure 15: Polarization-averaged Doppler frequency response for pulsar timing, where we have ignored the pulsar term. The response is axially symmetric around the z -axis, which we've chosen to be in the direction to the pulsar $\hat{p} = -\hat{u}$.

Here θ is the angle between \hat{k} and \hat{u} (which is the usual polar angle measured from the z -axis).

Note that if we include the pulsar term in the response, then $F^A(\hat{k})$ in (6.14) should be multiplied by a term proportional to $\sin(\pi fL[1 - \cos \theta]/c)$. This introduces a null at $\theta = 0$ and at other values of θ satisfying

$$\cos \theta = 1 - \frac{nc}{fL}, \quad n = 0, 1, \dots, \text{int}[2fL/c]. \quad (6.15)$$

In Figure 16 we show the full root-summed-squared response including the pulsar term, taking $fL/c = 20$ for illustration purposes. (For most pulsars, fL/c will be of order 100 or more, as the distance to typical pulsars is of order a kpc or more.) The response without the pulsar term (Figure 15) is also shown for comparison.

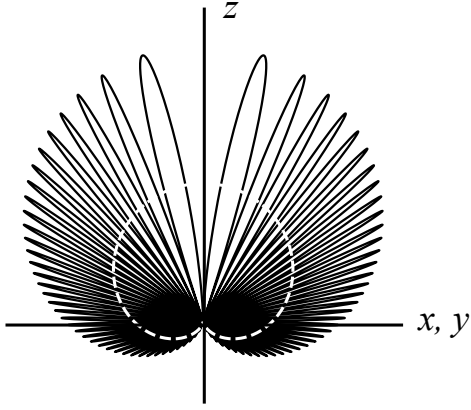


Figure 16: Same as Figure 15 but including the pulsar term and taking $fL/c = 20$. The response without the pulsar term is shown as a dashed-white curved for comparison.

6.3.2 Detector response for a laser interferometer in the short-antenna limit

Another simple example of a detector response function is for a equal-arm laser interferometer, like LIGO, in the *short-antenna* (or long-wavelength) approximation (Figure 17). This approximation is valid when the wavelength of the GW is much larger than the dimensions of the detector. The GW phase is then effectively constant as a photon travels down and back an interferometer arm.

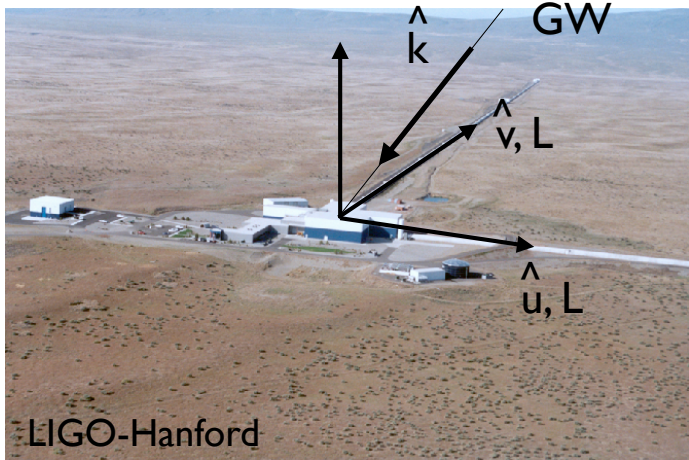


Figure 17: Geometry for a ground-based interferometer GW response calculation. (Shown here is the LIGO Hanford Observatory (LHO), in Hanford, WA.) The GW propagates in the \hat{k} direction; \hat{u} , \hat{v} are unit vectors that point along the two arms of the interferometer. In the short-antenna approximation, the length L of the arms does not enter the expression for the strain response.

The integral over the photon path is simply proportional to the nominal round-trip propagation time $2L/c$. Defining the strain response of the interferometer as

$$h(t) \equiv \frac{1}{2} \left(\frac{\Delta T_{\vec{u}, \text{roundtrip}}(t)}{T} - \frac{\Delta T_{\vec{v}, \text{roundtrip}}(t)}{T} \right), \quad (6.16)$$

one can show that

$$R^A(f, \hat{k}) \simeq \frac{1}{2} \left(u^a u^b - v^a v^b \right) e_{ab}^A(\hat{k}). \quad (6.17)$$

The quantity multiplying $e_{ab}^A(\hat{k})$ in the expression for the reponse function above is called the *detector tensor*

$$D^{ab} \equiv \frac{1}{2} \left(u^a u^b - v^a v^b \right). \quad (6.18)$$

Plots of the *beam pattern functions* $|R^+(f, \hat{k})|$ and $|R^\times(f, \hat{k})|$ for the two polarizations individually, and the root-summed-squared response (summed over both polarization) are shown in Figure 18. The last plot showing the root-summed-squared response is sometimes called the LIGO “peanut”. It illustrates that a laser-interferometer in the short-antenna approximation is a very blunt instrument, being sensitive to a very large portion of the sky. The only nulls are in the plane spanned by the arms, in the directions of the perpendicular bisectors of the arms.

7 Non-trivial correlations

In this section, we describe how to correlate the outputs of two detectors, taking into account their non-trivial response to GWs.

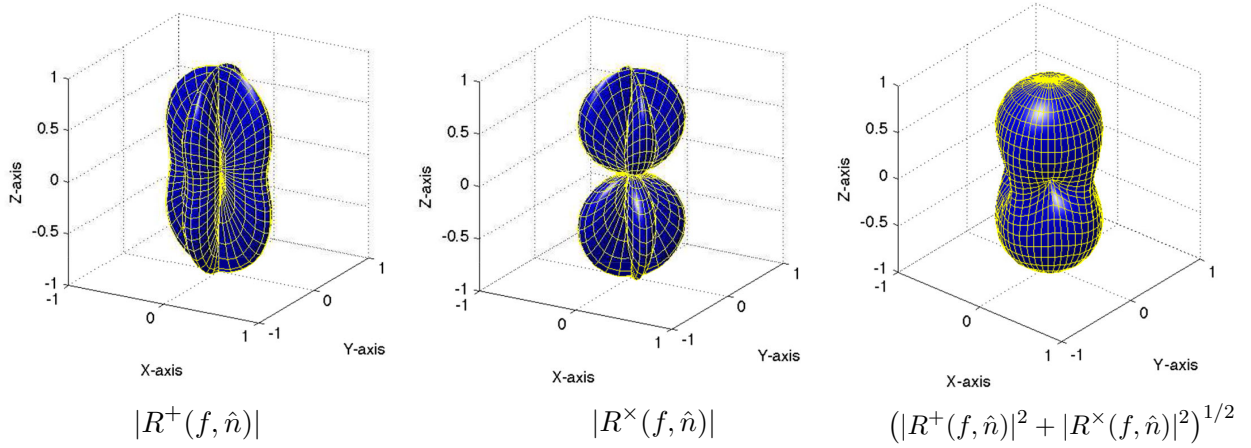


Figure 18: Beam pattern functions for a ground-based interferometer like LIGO in the short-antenna approximation—i.e., $f \lesssim$ few kHz. The vertex of the interferometer is at the origin of coordinates, and the interferometer arms are assumed to be orthogonal, pointing along the x and y directions.

7.1 Overlap function

Detectors in different locations and with different orientations respond differently to a passing GW. The *overlap function* encodes the reduction in sensitivity of a cross-correlation analysis due to the separation and misalignment of the detectors.

Let I and J label two detectors, and let $h_I(t)$ and $h_J(t)$ denote the corresponding response of these detectors to an unpolarized and isotropic GW background. The expected correlation of the two detector outputs can then be written as

$$\langle h_I(t)h_J(t') \rangle = \frac{1}{2} \int_{-\infty}^{\infty} df e^{i2\pi f(t-t')} \Gamma_{IJ}(f) S_h(f), \quad (7.1)$$

where $S_h(f)$ is the (1-sided) strain power spectral density of the GWB, cf. (3.5) and (3.9), and $\Gamma_{IJ}(f)$ is the overlap function:

$$\Gamma_{IJ}(f) = \frac{1}{8\pi} \int d^2\Omega_{\hat{k}} \sum_A R_I^A(f, \hat{k}) R_J^{A*}(f, \hat{k}). \quad (7.2)$$

Recall from (6.4), (6.5) that the location of the detector is already included in the response functions $R^A(f, \hat{k})$ via the phase factor $e^{-i2\pi\hat{k}\cdot\vec{x}/c}$. If we explicitly display this dependence by writing $R^A(f, \hat{k}) \equiv \bar{R}^A(f, \hat{k}) e^{-i2\pi f\hat{k}\cdot\vec{x}/c}$, then

$$\Gamma_{IJ}(f) = \frac{1}{8\pi} \int d^2\Omega_{\hat{k}} \sum_A \bar{R}_I^A(f, \hat{k}) \bar{R}_J^{A*}(f, \hat{k}) e^{-i2\pi f\hat{k}\cdot(\vec{x}_I - \vec{x}_J)/c}. \quad (7.3)$$

One often sees this alternative expression for $\Gamma_{IJ}(f)$ in the literature, e.g., [18, 12, 9].

The interpretation of $\Gamma_{IJ}(f)$ as encoding the reduction in sensitivity of a cross-correlation analysis due to the physical separation and relative orientation of the detectors is most easily seen in the frequency domain, where (7.1) becomes

$$\langle \tilde{h}_I(f) \tilde{h}_J^*(f') \rangle = \frac{1}{2} \delta(f - f') \Gamma_{IJ}(f) S_h(f). \quad (7.4)$$

From this expression, we see that $\Gamma_{IJ}(f)$ is a transfer function between the strain power $S_h(f)$ in the GWB and the detector cross-power $C_{IJ}(f) = \Gamma_{IJ}(f)S_h(f)$.

For statistically anisotropic backgrounds, it turns out that the integrand of $\Gamma_{IJ}(f)$ is the most important quantity for describing the cross-correlation. This is because for this case

$$\langle \tilde{h}_I(f)\tilde{h}_J^*(f') \rangle = \frac{1}{4}\delta(f-f') \int d^2\Omega_{\hat{k}} \sum_A R_I^A(f, \hat{k})R_J^{A*}(f, \hat{k})\mathcal{P}(f, \hat{k}), \quad (7.5)$$

where $\mathcal{P}(f, \hat{k})$ is the GW power on the sky, coming from direction $\hat{n} = -\hat{k}$; see (3.6) and (3.7). One typically expands $\mathcal{P}(f, \hat{k})$ in terms of spherical harmonics

$$\mathcal{P}(f, \hat{k}) = \sum_{l=0}^{\infty} \sum_{m=-l}^l \mathcal{P}_{lm}(f)Y_{lm}(\hat{k}), \quad (7.6)$$

for which (7.5) becomes

$$\langle \tilde{h}_I(f)\tilde{h}_J^*(f') \rangle = \frac{1}{2}\delta(f-f') \sum_{l=0}^{\infty} \sum_{m=-l}^l \Gamma_{IJ,lm}(f)\mathcal{P}_{lm}(f). \quad (7.7)$$

with [8, 52]

$$\Gamma_{IJ,lm}(f) \equiv \frac{1}{2} \int d^2\Omega_{\hat{k}} \sum_A R_I^A(f, \hat{k})R_J^{A*}(f, \hat{k})Y_{lm}(\hat{k}). \quad (7.8)$$

So up to a factor of $1/4\pi$, the spherical harmonic components of the integrand of the overlap function (7.2) encode the reduction in sensitivity when doing a cross-correlation for anisotropic backgrounds. Interested readers can find much more discussion about anisotropic backgrounds in Section 7 of [41], and references to the original work cited therein.

7.2 Examples

Given (7.2) for $\Gamma_{IJ}(f)$ and explicit expressions for the response functions $R_J^A(f, \hat{k})$ for different detectors, we can now calculate the overlap function for different detector pairs.

7.2.1 Overlap function for a pair of laser interferometers in the short-antenna limit

Our first example will be the overlap function for pairs of laser interferometers in the short-antenna approximation. For concreteness, we will consider the LIGO Hanford-LIGO Livingston detector pair (which we will denote LHO-LLO) and the LIGO Hanford-Virgo (LHO-Virgo) detector pair. Plots of these overlap functions, normalized to unity for coincident and coaligned detectors (denoted $\gamma(f)$) are shown in Figure 19.

For the LHO-LLO detector pair, note that as $f \rightarrow 0$, $\gamma(f) \rightarrow -0.89$. The minus sign indicates that the two interferometers are rotated by 90° relative to one another. The fact that the absolute value $|\gamma(0)| = 0.89$ is not exactly equal to 1, even though the overlap function is normalized, indicates that the two interferometers aren't exactly (anti) aligned. The two interferometers are separated by 27.2° as seen from the center of the Earth, so the tangent planes of the interferometers are tilted relative to one another due to the curvature of the Earth. In addition, the first zero crossing of the overlap function occurs at approximately 60 Hz, which corresponds (roughly) to the frequency (50 Hz) of a GW having a wavelength equal to twice the separation (2×3000 km)

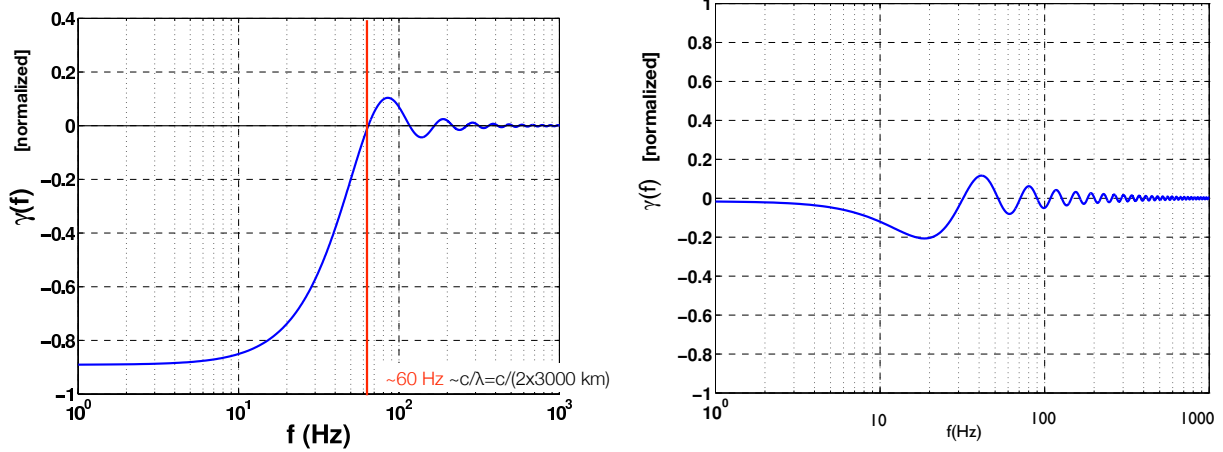


Figure 19: Normalized overlap function for ground-based interferometers calculated in the short-antenna approximation. Left panel: LHO-LLO overlap function. Right panel: LHO-Virgo overlap function.

between the two observatories. For lower frequencies, the two interferometers are driven (on average) by the same positive (or negative) part of a passing GW; while for slightly larger frequencies, the two interferometers start to be driven by parts of the GW having opposite signs. The zero crossings correspond to the transitions between these in-phase and out-of-phase excitations of the interferometers.

For the LHO-Virgo detector pair, note that in the limit $f \rightarrow 0$, $\gamma(f) \simeq 0$. This is because the two interferometers effectively respond to the two orthogonal polarizations of a GW, corresponding to a rotation of the interferometer arms by 45° . This 45° misalignment is also the reason for the (overall) reduced amplitude of the LHO-Virgo overlap function relative to that for LHO-LLO. The fact that the first zero crossing for the LHO-Virgo overlap function is just over 30 Hz (almost half that for LHO-LLO) is due the larger separation between the LHO and Virgo interferometers, compared to LHO and LLO.

7.2.2 Overlap function for pulsar timing arrays

If one uses (6.12) for the Doppler frequency response of a pulsar timing measurement, then the correlation between two Earth-pulsar baselines is just a single number as the response functions $F_{I,J}^A(\hat{k})$ are independent of frequency. This number, which can be interpreted as the expected correlation between the two pulsar timing measurements, depends on the angular separation between the two Earth-pulsar baselines [24]:

$$\chi(\zeta_{IJ}) \equiv \frac{1}{2} + \frac{3}{2} \left(\frac{1 - \cos \zeta_{IJ}}{2} \right) \left[\ln \left(\frac{1 - \cos \zeta_{IJ}}{2} \right) - \frac{1}{6} \right] + \frac{1}{2} \delta_{IJ}, \quad (7.9)$$

where $\zeta_{IJ} = \cos^{-1}(\hat{p}_I \cdot \hat{p}_J)$, with $\hat{p}_{I,J}$ being unit vectors pointing in the directions to the pulsars ($\hat{p} = -\hat{u}$ in the notation of (6.12)). A plot of this expected correlation as a function of the angular separation between the Earth-pulsar baselines is shown in Figure 20. This is called the *Hellings and Downs curve*, originally calculated in 1983 by Hellings and Downs [24]. This calculation assumes that the GWB is unpolarized and isotropic. Generalizations of the Hellings-Downs curve allowing for anisotropy and non-general-relativity polarization modes can be found in e.g., [33, 19, 30, 11, 20].

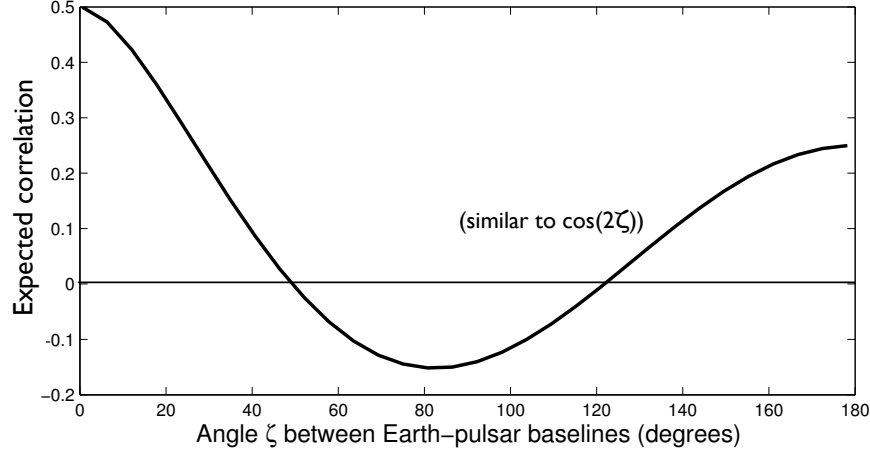


Figure 20: Hellings and Downs curve. Plotted are the values of the expected correlation for an unpolarized, isotropic GWB as a function of the angle ζ between two Earth-pulsar baselines.

The quadrupolar nature of GWs in general relativity is apparent in the Hellings-Down curve, with an angular dependence that is qualitatively similar to $\cos(2\zeta)$, where ζ is the angle between two Earth-pulsar baselines.

The fact that $\chi(0^\circ)$ is twice as large as $\chi(180^\circ)$ can easily be demonstrated by using (6.14) for the relevant response functions. Taking the two pulsars to point in the same direction ($\hat{p}_1 = \hat{p}_2 = \hat{z}$), we have

$$\sum_A F_1^A(\hat{k})F_2^A(\hat{k}) = \frac{1}{4}(1 + \cos \theta)^2, \quad (7.10)$$

while having them point in opposite directions ($\hat{p}_1 = -\hat{p}_2 = \hat{z}$) leads to

$$\sum_A F_1^A(\hat{k})F_2^A(\hat{k}) = \frac{1}{4}(1 + \cos \theta)(1 - \cos \theta) = \frac{1}{4} \sin^2 \theta. \quad (7.11)$$

These functions are plotted in Figure 21, where θ is the usual polar angle measured with respect to the z -axis. Multiplying by $1/8\pi$ and integrating over the sphere, we find:¹²

$$\Gamma_{12} = \frac{1}{6} \quad (\text{for } \hat{p}_1 = \hat{p}_2 = \hat{z}), \quad \Gamma_{12} = \frac{1}{12} \quad (\text{for } \hat{p}_1 = -\hat{p}_2 = \hat{z}). \quad (7.12)$$

From Figure 21, we see that when the two pulsars both point in the \hat{z} direction, the majority of support for the overlap function comes from sky directions $\hat{n} = -\hat{k}$ having $z > 0$. When the two pulsars point in opposite directions, $\hat{p}_1 = -\hat{p}_2 = \hat{z}$, the majority of support for the overlap function comes from sky directions in the xy -plane, which is a smaller contribution.

7.2.3 Overlap function for a pair of electric dipole antennae

For the final example, you are asked in Exercise A.7 to calculate the overlap function for a pair of short, colocated electric dipole antennae in the presence of an unpolarized and isotropic electric field $\vec{E}(t, \vec{x})$; see also [26]. The two dipole antennae point in different directions separated by an angle ζ as shown in Figure 22. To do the calculation, you should use the fact that the response of

¹²The factor of 3 difference between these two values for Γ_{12} and $\chi(0^\circ) = 1/2$ and $\chi(180^\circ) = 1/4$ is due to a normalization factor that is conventionally applied to relate Γ_{IJ} to $\chi(\zeta_{IJ})$.

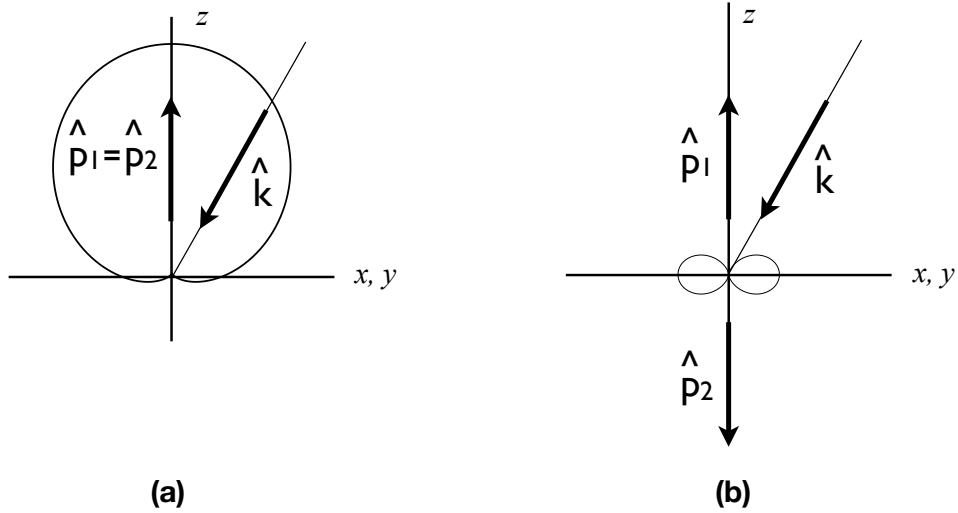


Figure 21: Graphical representation of the integrand of the (Earth-only) overlap function for pulsar timing Doppler frequency measurements. Panel (a): integrand for two Earth-pulsar baselines having $\zeta = 0^\circ$ ($\hat{p}_1 = \hat{p}_2 = \hat{z}$); Panel (b): integrand for two Earth-pulsar baselines having $\zeta = 180^\circ$ ($\hat{p}_1 = -\hat{p}_2 = \hat{z}$). These functions are axially symmetric around the z -axis, which we've chosen to be in the direction to pulsar 1.

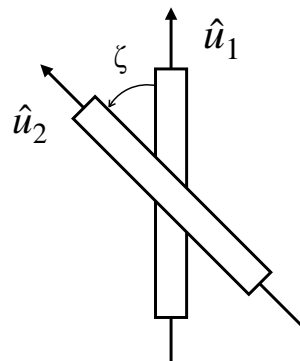


Figure 22: Geometry for calculating the overlap function for a pair of short, colocated electric dipole antennae, for an unpolarized and isotropic electric field (Exercise A.7).

dipole antenna I to the electric field is

$$r_I(t) = \hat{u}_I \cdot \vec{E}(t, \vec{x}_0). \quad (7.13)$$

The electric field can be expanded in a manner similar to that for an unpolarized, isotropic GWB:

$$\vec{E}(t, \vec{x}) = \int_{-\infty}^{\infty} df \int d^2\Omega_{\hat{k}} \sum_{\alpha=1}^2 \tilde{E}_{\alpha}(f, \hat{k}) \hat{\epsilon}_{\alpha}(\hat{k}) e^{i2\pi f(t - \hat{k} \cdot \vec{x}/c)}, \quad (7.14)$$

where the polarization vectors are given by

$$\hat{\epsilon}_1(\hat{k}) = \hat{\theta}, \quad \hat{\epsilon}_2(\hat{k}) = \hat{\phi}. \quad (7.15)$$

In addition, the Fourier components $\tilde{E}_{\alpha}(f, \hat{k})$ satify the quadratic expectation values, cf. (3.5):

$$\langle \tilde{E}_{\alpha}(f, \hat{k}) \tilde{E}_{\alpha'}^*(f', \hat{k}') \rangle = \frac{1}{16\pi} S_E(f) \delta(f - f') \delta_{\alpha\alpha'} \delta^2(\hat{k}, \hat{k}'). \quad (7.16)$$

With these definitions, it is then just a matter of “turning the crank” to calculate the expectation value $\langle r_1(t)r_2(t') \rangle$, and from that you can read off the overlap function $\Gamma_{12}(f)$ according to (7.1). You should find

$$\Gamma_{12}(f) = \frac{2}{3} \hat{u}_1 \cdot \hat{u}_2 = \frac{2}{3} \cos \zeta. \quad (7.17)$$

The dipole nature of the antennae shows up in the $\cos \zeta$ dependence of the overlap function.

8 Statistical inference

In order to discuss our final example (Section 9), which is an optimal search for the popcorn-like background produced by stellar-mass BBH mergers throughout the universe, we need to go beyond the frequentist statistics that we have used so far (Section 4), and introduce some concepts from the field of Bayesian inference. So here, we briefly introduce Bayesian inference by comparing it to frequentist statistics, focusing mainly on those topics needed for the stochastic search that we shall describe in Section 9. Readers who are interested in more details should consult John Veitch’s contribution to this Volume, Section 3 of [41], and e.g., [21].

8.1 Comparing frequentist statistics and Bayesian inference

We start by listing the key ingredients of these two formulations of statistical inference.

Frequentist statistics:

- probabilities are long-run relative occurrence of outcomes of repeatable experiments (i.e., random variables); probabilities cannot be assigned to hypotheses or parameters, which have fixed but unknown values.
- one usually starts by writing down a likelihood function $p(d|H)$, which is the probability distribution for the measured data d , assuming the truth of a particular hypothesis H .
- to estimate the value of parameters and/or to decide between different hypotheses, one constructs *statistics*, which are particular functions of the data.

- to make probabilistic statements about parameter estimates or hypothesis testing, one needs to calculate the probability distributions of the statistics; this can be done either analytically or numerically (e.g., using time slides to produce different realistic noise realizations of the data).
- given the probability distributions of the statistics, one can then construct confidence intervals and p -values (the probability of obtaining a detection statistic value as large or larger than what was measured) for parameter estimation and hypothesis testing.

Bayesian inference:

- probability is degree of belief (or confidence) in any proposition, and hence can be assigned to hypotheses and parameters. (This is a more general definition of probability than that used in frequentist statistics.)
- like a frequentist, one usually starts by writing down a likelihood function $p(d|H)$.
- in addition to the likelihood function, one needs to specify prior probability distributions for the various parameters and hypotheses that one is considering.
- one uses Bayes' theorem to update the prior degree of belief in a parameter value or hypothesis in light of new data.
- one constructs posterior distributions and odds ratios (or *Bayes factors*, see Section 8.3.1) for parameter estimation and hypothesis testing (also called model selection).

In a nutshell, the main difference between Bayesian and frequentist statistics is the definition of probability. As such, certain probabilistic statements that you can make as a Bayesian are not valid from a frequentist perspective. Hence, Bayesian and frequentist statistics often ask (and subsequently answer) *different* questions about the data. Nonetheless, despite this fundamental difference in approach, if the data are sufficiently informative (i.e., if the likelihood is peaked relative to the prior distributions for the parameters, see Figure 24), then both Bayesian and frequentist analyses give more or less consistent results.

8.1.1 Likelihood functions

As mentioned above, the starting point for most frequentist and Bayesian analyses is a likelihood function, which we can write schematically as

$$\text{likelihood} = p(\text{data}|\text{parameters, model}). \quad (8.1)$$

For example, for Gaussian-distributed detector noise and a Gaussian-distributed GWB, the likelihood function for the noise-only model \mathcal{M}_0 and signal+noise model \mathcal{M}_1 are given by

$$p(d|S_{n_1}, S_{n_2}, \mathcal{M}_0) = \frac{1}{\sqrt{\det(2\pi C_n)}} \exp\left[-\frac{1}{2}d^T C_n^{-1} d\right], \quad (8.2)$$

$$p(d|S_{n_1}, S_{n_2}, S_h, \mathcal{M}_1) = \frac{1}{\sqrt{\det(2\pi C)}} \exp\left[-\frac{1}{2}d^T C^{-1} d\right], \quad (8.3)$$

where C_n and C are the covariance matrices for the noise-only and signal+noise models, respectively. For N samples of white noise and white GWB in two colocated and coaligned detectors:

$$C_n = \begin{bmatrix} S_{n_1} \mathbf{1}_{N \times N} & \mathbf{0}_{N \times N} \\ \mathbf{0}_{N \times N} & S_{n_2} \mathbf{1}_{N \times N} \end{bmatrix}, \quad C = \begin{bmatrix} (S_{n_1} + S_h) \mathbf{1}_{N \times N} & S_h \mathbf{1}_{N \times N} \\ S_h \mathbf{1}_{N \times N} & (S_{n_2} + S_h) \mathbf{1}_{N \times N} \end{bmatrix}, \quad (8.4)$$

where $\mathbf{1}_{N \times N}$ and $\mathbf{0}_{N \times N}$ denote the unit matrix and zero matrix, respectively, in N dimensions. For this simple case, there are only three relevant parameters: S_{n_1} , S_{n_2} for the detector noise, and S_h for the GWB. Also, by assuming that the detectors are colocated and coaligned, we don't have to worry about including an overlap function in the off-diagonal blocks of the signal+noise covariance matrix C .

8.2 Frequentist analyses

Starting from the likelihood functions for the noise-only and signal+noise models, we can construct the *maximum-likelihood ratio* statistic:

$$\Lambda_{\text{ML}}(d) \equiv \frac{\max_{S_{n_1}, S_{n_2}, S_h} p(d|S_{n_1}, S_{n_2}, S_h, \mathcal{M}_1)}{\max_{S_{n_1}, S_{n_2}} p(d|S_{n_1}, S_{n_2}, \mathcal{M}_0)}. \quad (8.5)$$

The values of the parameters that maximize the likelihood for the signal+noise model can be used as frequentist estimators of the true values of the parameters S_{n_1} , S_{n_2} , S_h . In Exercise A.8 you are asked to show that the data combinations

$$\hat{C}_{11} \equiv \frac{1}{N} \sum_{i=1}^N d_{1i}^2, \quad \hat{C}_{22} \equiv \frac{1}{N} \sum_{i=1}^N d_{2i}^2, \quad \hat{C}_{12} \equiv \frac{1}{N} \sum_{i=1}^N d_{1i} d_{2i}, \quad (8.6)$$

are maximum-likelihood estimators of

$$S_1 \equiv S_{n_1} + S_h, \quad S_2 \equiv S_{n_2} + S_h, \quad S_h. \quad (8.7)$$

Note that the maximum-likelihood estimator $\hat{S}_h \equiv \hat{C}_{12}$ of S_h is just the standard cross-correlation statistic introduced in (4.7). The maximum-likelihood estimators of the detector noise S_{n_1} , S_{n_2} are then

$$\hat{S}_{n_1} \equiv \hat{S}_1 - \hat{S}_h = \hat{C}_{11} - \hat{C}_{12}, \quad \hat{S}_{n_2} \equiv \hat{S}_2 - \hat{S}_h = \hat{C}_{22} - \hat{C}_{12}. \quad (8.8)$$

In addition, in Exercise A.9, you are asked to show that

$$\Lambda(d) \equiv 2 \ln(\Lambda_{\text{ML}}(d)) \simeq \frac{\hat{C}_{12}^2}{\hat{C}_{11} \hat{C}_{22}/N}, \quad (8.9)$$

which holds in the weak-signal approximation, where $S_h \ll S_{n_1}, S_{n_2}$. The quantity $\Lambda(d)$ can be used as a frequentist detection statistic, comparing its value for the given data d to a threshold Λ_* . If $\Lambda(d) \geq \Lambda_*$, we reject the null hypothesis (the noise-only model) and claim detection of a GW signal; if $\Lambda(d) < \Lambda_*$, we accept the null-hypothesis and reject the signal+noise hypothesis. Note that the right-hand-side of (8.9) is the square of the (power) signal-to-noise ratio, cf. (4.13), which illustrates a useful general relation between signal-to-noise ratios and the maximum-likelihood statistic.

8.3 Bayesian analyses

Not surprisingly, Bayesian analyses make use of Bayes' theorem:

$$p(H|d) = \frac{p(d|H)p(H)}{p(d)}, \quad (8.10)$$

which converts probabilities about the data d given a hypothesis H (the likelihood $p(d|H)$) to probabilities about the hypothesis given the data (the posterior distribution $p(H|d)$).¹³ Here, $p(H)$ is the prior probability distribution for H , and $p(d)$ is the *evidence* or *marginalized likelihood*:

$$p(d) \equiv \int dH p(d|H)p(H). \quad (8.11)$$

Note that the evidence is simply the normalization factor needed to insure $\int dH p(H|d) = 1$. The importance of Bayes' theorem is that it updates our degree of belief in a hypothesis in light of new data. It maps the prior probability $p(H)$ to the posterior probability $p(H|d)$ via the likelihood function $p(d|H)$ (Figure 23).

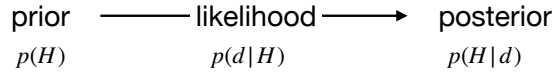


Figure 23: Schematic representation of Bayes' theorem.

In the context of searches for stochastic GW backgrounds, Bayes' theorem has the form:

$$p(S_{n_1}, S_{n_2}, S_h|d, \mathcal{M}_1) = \frac{p(d|S_{n_1}, S_{n_2}, S_h, \mathcal{M}_1)p(S_{n_1}, S_{n_2}, S_h|\mathcal{M}_1)}{p(d|\mathcal{M}_1)}, \quad (8.12)$$

where $p(d|S_{n_1}, S_{n_2}, S_h, \mathcal{M}_1)$ is the likelihood function (8.3). Here \mathcal{M}_1 is our signal+noise model and S_{n_1} , S_{n_2} , S_h are the parameters describing this model. The quantity $p(S_{n_1}, S_{n_2}, S_h|d, \mathcal{M}_1)$ is the *joint* posterior probability distribution for the parameters S_{n_1} , S_{n_2} , S_h of model \mathcal{M}_1 given the data d . The posterior distribution for S_h alone is given by integrating over S_{n_1} , S_{n_2} :

$$p(S_h|d, \mathcal{M}_1) = \int dS_{n_1} \int dS_{n_2} p(S_{n_1}, S_{n_2}, S_h|d, \mathcal{M}_1). \quad (8.13)$$

8.3.1 Bayes factors and model selection

To assess which of two models \mathcal{M}_0 , \mathcal{M}_1 is more consistent with the observed data d , we form the ratio of the posterior distributions $p(\mathcal{M}_0|d)$, $p(\mathcal{M}_1|d)$. Using Bayes' theorem, we obtain

$$\frac{p(\mathcal{M}_1|d)}{p(\mathcal{M}_0|d)} = \frac{p(d|\mathcal{M}_1)p(\mathcal{M}_1)}{p(d|\mathcal{M}_0)p(\mathcal{M}_0)}, \quad (8.14)$$

where the common evidence term $p(d)$ in (8.10) has canceled out when taking the ratio of the two posteriors. Thus, we see that the posterior odds ratio $O_{10}(d) \equiv p(\mathcal{M}_1|d)/p(\mathcal{M}_0|d)$ is equal to the prior odds ratio $O_{10} \equiv p(\mathcal{M}_1)/p(\mathcal{M}_0)$ times the *Bayes factor*

$$\mathcal{B}_{10}(d) \equiv \frac{p(d|\mathcal{M}_1)}{p(d|\mathcal{M}_0)}. \quad (8.15)$$

¹³Conditional probabilities $p(A|B)$ and $p(B|A)$ are not equal in general. Paraphrasing an example from Louis Lyons: the probability that a person is pregnant (A) given that that person is a woman (B) is about about 30%; while the probability that a person is a woman (B) given that that person is pregnant (A) is 100%.

The numerator and denominator in the Bayes factor are the marginalized likelihoods obtained by marginalizing the full likelihood functions $p(d|\theta_\alpha, \mathcal{M}_\alpha)$ over the model parameters θ_α :

$$p(d|\mathcal{M}_\alpha) \equiv \int d\theta_\alpha p(d|\theta_\alpha, \mathcal{M}_\alpha) p(\theta_\alpha|\mathcal{M}_\alpha), \quad (8.16)$$

where $\alpha = 0, 1$ labels the two models. If there is no *a priori* reason prefer one model over the other (i.e., if the prior odds ratio $O_{10} = 1$), then the posterior odds ratio for the two models is equal to the Bayes' factor, $O_{10}(d) = \mathcal{B}_{10}(d)$.

Using the above definitions, we are now in a position to relate Bayesian and frequentist inference, at least in the case where the data are informative. By this we mean that the likelihood function for a given model is peaked relative to the prior probability distribution for its model parameters (Figure 24). For this case, the marginalized likelihoods functions have the approximate form

$$p(d|\mathcal{M}_\alpha) \simeq p(d|\hat{\theta}_\alpha, \mathcal{M}_\alpha) \Delta V_\alpha / V_\alpha, \quad (8.17)$$

where $\hat{\theta}_\alpha$ denote the parameter values that maximize the likelihood, ΔV_α is the range of parameter values over which the likelihood is peaked, and V_α denotes the full parameter volume. This approximation is called the *Laplace approximation*. Substituting these expressions into (8.15) we

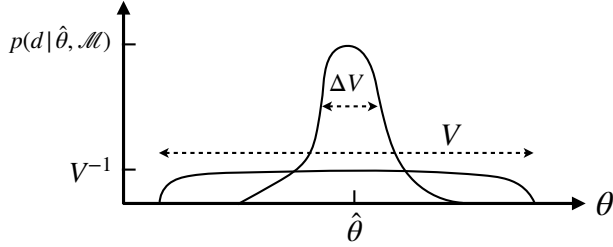


Figure 24: Schematic representation of the likelihood function $p(d|\theta, \mathcal{M})$ and prior probability distribution $p(\theta|\mathcal{M})$ for the model parameters θ , when the data d are informative. In this case, the likelihood function is peaked relative to the prior probability distribution, with maximum at $\theta = \hat{\theta}$ and characteristic width ΔV . The full parameter space volume is denoted by V .

find

$$\mathcal{B}_{10}(d) \equiv \frac{p(d|\mathcal{M}_1)}{p(d|\mathcal{M}_0)} \simeq \frac{p(d|\hat{\theta}_1, \mathcal{M}_1)}{p(d|\hat{\theta}_0, \mathcal{M}_0)} \frac{\Delta V_1/V_1}{\Delta V_0/V_0} \simeq \Lambda_{\text{ML}}(d) \frac{\Delta V_1/V_1}{\Delta V_0/V_0}, \quad (8.18)$$

where $\Lambda_{\text{ML}}(d)$ is just the maximum-likelihood ratio for the two models. This last expression can also be written as

$$2 \ln(\mathcal{B}_{10}(d)) \simeq \Lambda(d) + 2 \ln \left(\frac{\Delta V_1/V_1}{\Delta V_0/V_0} \right) \quad (8.19)$$

where $\Lambda(d) \equiv 2 \ln(\Lambda_{\text{ML}}(d))$ plays the role of a frequentist detection statistic, and the last term is an Occam's factor that penalizes models that use more parameter space volume than needed to fit the data. As shown in (8.9), $\Lambda(d)$ is effectively a squared signal-to-noise ratio. The key observation here is that the ratio of marginalized likelihoods, i.e., the Bayes factor, is well approximated by a maximum-likelihood ratio times an Occam's penalty factor when the data are informative.

8.3.2 Bayesian signal priors

The final piece of information that we will need for discussing the Bayesian search in Section 9 is the choice of signal prior. We shall see in that section that by choosing the signal prior appropriately, we can properly model the popcorn-like nature of GW background produced by stellar-mass BBH mergers throughout the universe.

Here we illustrate the effect of choosing different priors for two simple cases: (i) a deterministic GW signal (a sinusoid), and (ii) a Gaussian-stationary stochastic background in Gaussian-distributed noise. For both of these cases, the difference between the observed data d and signal model h is the noise n . So we can write down a generic likelihood function for the data d by equating it to the Gaussian-distributed noise likelihood for the residuals $d - h$:

$$p(d|C_n, h) \equiv p_n(d - h|C_n) = \frac{1}{\sqrt{\det(2\pi C_n)}} \exp \left[-\frac{1}{2}(d - h)^T C_n^{-1}(d - h) \right], \quad (8.20)$$

where C_n is the noise covariance matrix. To proceed further we need to specify the form of the signal h .

(i) For a deterministic GW signal, we expect the signal samples to have a precise form, e.g., a sine wave parametrized by its amplitude, frequency, and initial phase (Figure 25(a)). For this case the signal prior is Dirac delta function that sets the signal samples to the model waveform,

$$p(h|A, f_0, \phi_0) = \delta(h(t) - A \sin(2\pi f_0 t + \phi_0)). \quad (8.21)$$

Multiplying the likelihood (8.20) by this prior and then (trivially) marginalizing over the signal samples h yields

$$\begin{aligned} p(d|C_n, A, f_0, \phi_0) &\equiv \int dh p_n(d - h|C_n)p(h|A, f_0, \phi_0) \\ &= \frac{1}{\sqrt{\det(2\pi C_n)}} \exp \left[-\frac{1}{2} \sum_{i,j} (d_i - A \sin(2\pi f_0 t_i + \phi_0)) [C_n^{-1}]_{ij} (d_j - A \sin(2\pi f_0 t_j + \phi_0)) \right]. \end{aligned} \quad (8.22)$$

This marginalized likelihood function with priors on the range of parameter values for A, f_0, ϕ_0 (for the signal) and the covariance matrix C_n (for the noise) then completely defines the deterministic signal+noise model.



Figure 25: Different signal priors for $h(t)$. Panel (a): Deterministic (sinusoid) signal prior. Panel (b): Stochastic signal prior. For the stochastic signal prior, $h(t)$ values are drawn from a Gaussian distribution with variance S_h .

(ii) For a stochastic GW signal, we cannot predict with certainty what the individual samples h will be; we can only say that they are drawn from some probability distribution. Taking that distribution to be a Gaussian with zero mean and variance S_h (Figure 25(b)), we have

$$p(h|S_h) = \frac{1}{\sqrt{2\pi S_h}} \exp\left[-\frac{1}{2} \frac{h^2}{S_h}\right]. \quad (8.23)$$

So multiplying the likelihood (8.20) by this prior and marginalizing over the signal samples h yields for this case

$$p(d|C_n, S_h) \equiv \int dh p_n(d - h|C_n) p(h|S_h) = \frac{1}{\sqrt{\det(2\pi C)}} \exp\left[-\frac{1}{2} d^T C^{-1} d\right], \quad (8.24)$$

where $C \equiv C_n + S_h$. This marginalized likelihood with a prior on the variance S_h for the stochastic signal samples and covariance matrix C_n for the noise then completely defines the Gaussian-stationary stochastic signal+noise model.

In Exercise A.10 you are asked to extend the above analysis for a stochastic background to the case of two coincident and coaligned detectors with uncorrelated detector noise. You should start with the generic two-detector likelihood function

$$p(d|C_n, h) \equiv p_n(d - h|C_n) = \frac{1}{\sqrt{\det(2\pi C_n)}} \exp\left[-\frac{1}{2} (d - h)^T C_n^{-1} (d - h)\right], \quad (8.25)$$

where

$$C_n = \begin{bmatrix} S_{n_1} & 0 \\ 0 & S_{n_2} \end{bmatrix}, \quad (8.26)$$

and then marginalize over h using (8.23). The final result should be

$$p(d|C_n, S_h) = \frac{1}{\sqrt{\det(2\pi C)}} \exp\left[-\frac{1}{2} d^T C^{-1} d\right], \quad (8.27)$$

where

$$C = \begin{bmatrix} S_{n_1} + S_h & S_h \\ S_h & S_{n_2} + S_h \end{bmatrix}. \quad (8.28)$$

Note that the stochastic background contributes to both the diagonal and off-diagonal components of the covariance matrix. (The overlap function doesn't appear since we have assumed coincident and coaligned detectors.) This marginalized likelihood is usually taken as the starting point for all stochastic cross-correlation searches using multiple detectors; see (8.3).

9 Searching for the background of binary black-hole mergers

As discussed in Section 1.2, the non-continuous popcorn-like background from BBH mergers is a potential signal for the advanced LIGO and Virgo network of detectors. The recent detections of several large signal-to-noise ratio BBH and BNS mergers imply the existence of a stochastic GW background composed of the more distant, weaker events. In 2018, Smith & Thrane [47] proposed an alternative to the standard cross-correlation method (Section 4) to search for the BBH component, optimally suited for the popcorn-nature of the signal. This was done by describing the BBH background with a “mixture” signal prior consisting of a BBH chirp in a certain fraction ξ of the analyzed segments, and just noise for the remaining segments. Also, as the individual signals will not be resolvable, they choose to marginalize over the BBH chirp parameters leaving only the probability parameter ξ (which is simply related to the rate of BBH merger signals) to estimate. Although in principle they can do the analysis with a single detector, they use two detectors to help discriminate against glitches.

9.1 Analysis details

The key components of their analysis are as follows:

- 1) Begin by splitting the data into short (e.g., 4 sec) segments, $i = 1, 2, \dots, N_{\text{seg}}$, which should contain at most one BBH merger signal.
- 2) Choose a *mixture* signal prior for the signal model:

$$p(h|\xi, \vec{\lambda}) = \xi \delta\left(h - \text{chirp}(\vec{\lambda})\right) + (1 - \xi) \delta(h), \quad (9.1)$$

which consists of a BBH chirp signal with probability ξ and just noise ($h = 0$) with probability $(1 - \xi)$ (Figure 26). This mixture signal prior captures the non-continuous popcorn-like nature of the BBH mergers.



Figure 26: The two components of the mixture signal prior for the Bayesian BBH merger search. Panel (a): With probability ξ , the signal prior for $h(t)$ is a chirp waveform. Panel (b): With probability $(1 - \xi)$, the signal prior for $h(t)$ is just noise, i.e., $h(t) = 0$.

- 3) For each segment of data d_i , marginalize the generic likelihood function

$$p(d_i|C_n, h) \equiv p_n(d_i - h|C_n) \quad (9.2)$$

over the signal samples h using the signal prior (9.1):

$$\begin{aligned} p(d_i|\xi, \vec{\lambda}, C_n) &= \int dh p(d_i|C_n, h)p(h|\xi, \vec{\lambda}) \\ &= \xi p_n(d_i - \text{chirp}(\vec{\lambda})|C_n) + (1 - \xi) p_n(d_i|C_n). \end{aligned} \quad (9.3)$$

Note that this is a mixture-Gaussian likelihood function.

- 4) Further marginalize over the BBH signal parameters $\vec{\lambda}$, and use an estimate of the detector noise thus fixing $C_n \equiv \bar{C}_n$:

$$p(d_i|\xi) = \int d\vec{\lambda} p(d_i|\xi, \vec{\lambda}, \bar{C}_n) p(\vec{\lambda}) \equiv (S_i - N_i)\xi + N_i, \quad (9.4)$$

where $N_i \equiv p(d_i|\bar{C}_n)$ and $S_i \equiv \int d\vec{\lambda} p(d_i|\xi, \vec{\lambda}, \bar{C}_n) p(\vec{\lambda})$.

- 5) Calculate the posterior for each segment using Bayes' theorem

$$p(\xi|d_i) = \frac{p(d_i|\xi)p(\xi)}{p(d_i)}, \quad (9.5)$$

taking $p(\xi) = \text{const.}$

6) Finally, combine segments by multiplying the individual marginalized likelihoods

$$p(d|\xi) = \prod_i p(d_i|\xi). \quad (9.6)$$

The final posterior distribution $p(\xi|d)$ is proportional to the product of the individual segment posteriors $p(\xi|d_i)$ since $p(\xi) = \text{const}$.

9.2 Illustrating the analysis method on simulated data

We now illustrate the method on some simulated toy-model data.¹⁴ The simulated time-series for the two detectors are each only 10 s long, and our simulated BBH chirps are less than 0.25 sec in duration. (Since this is only a toy-model, I didn't worry about making it astrophysically realistic.)

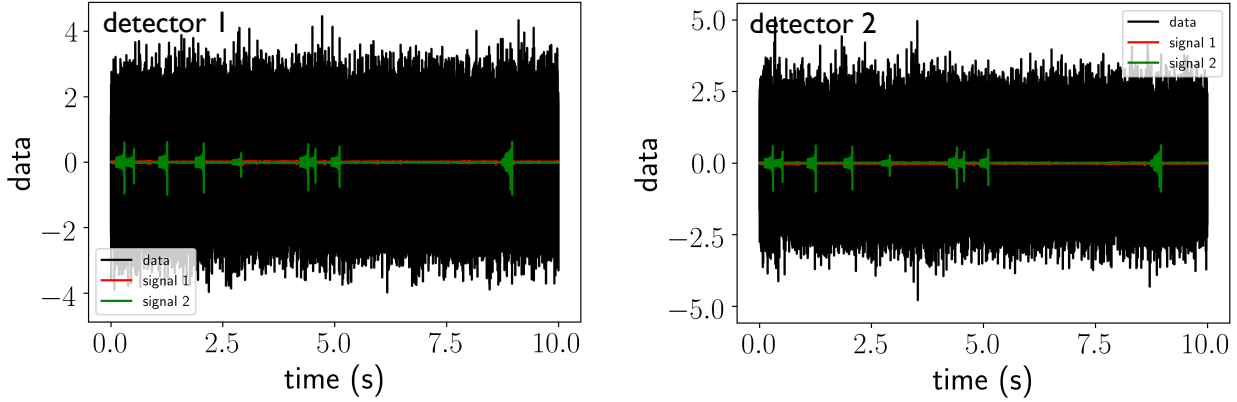


Figure 27: Simulated BBH and BNS data in two coincident and coaligned detectors. The confusion-limited BNS background is shown in orange; the popcorn-like BBH background is shown in green. The black trace is the data consisting of the BBH and BNS signals plus white Gaussian-stationary noise, uncorrelated in the two detectors.

We divided the simulated data into 40 segments (each of duration 0.25 s), and we injected 10 signals into uncorrelated white Gaussian noise in two coincident and coaligned detectors, corresponding to a injected value of the probability parameter $\xi = 0.25$ (Figure 27). The signal parameters $\vec{\lambda}$ that we marginalized over were just the amplitude and time of arrival of a BBH chirp in each segment. We assumed that we knew the shape and duration of the signal.

The final result of the analysis is the posterior distribution for ξ , shown in Figure 28. One sees that it is peaked around the value of ξ used for the injections, $\xi = 0.25$. Figure 29 shows the posterior distributions for ξ for the first 16 segments (first 4 sec) of data. Note that these distributions are all linear in ξ , as to be expected from (9.4) for the individual-segment likelihood functions. In addition, the cumulative posterior distributions for ξ , obtained by combining the likelihood functions for the first n segments of data are shown in Figure 30 for $n = 1, 2, 3, 4, 10, 20, 30$, and 40 segments. As n increases, the product of the individual linear functions of ξ , some with positive slope (when there is evidence in favor of the presence of a signal) and some with negative slope (when there is evidence in favor of the absence of a signal), give rise to a distribution that gets more and more peaked. The bottom-rightmost plot is just the final posterior distribution shown in Figure 28.

¹⁴The simulated data and analysis routines are publicly available at [57].

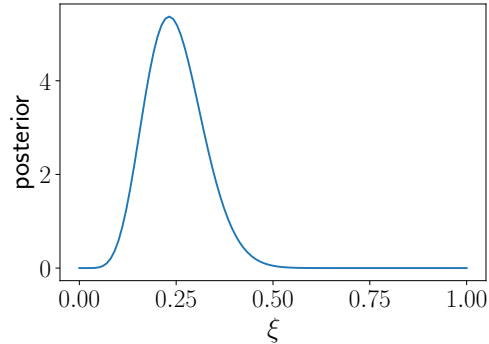


Figure 28: The cumulative posterior distribution for ξ after combining all 40 segments of data.

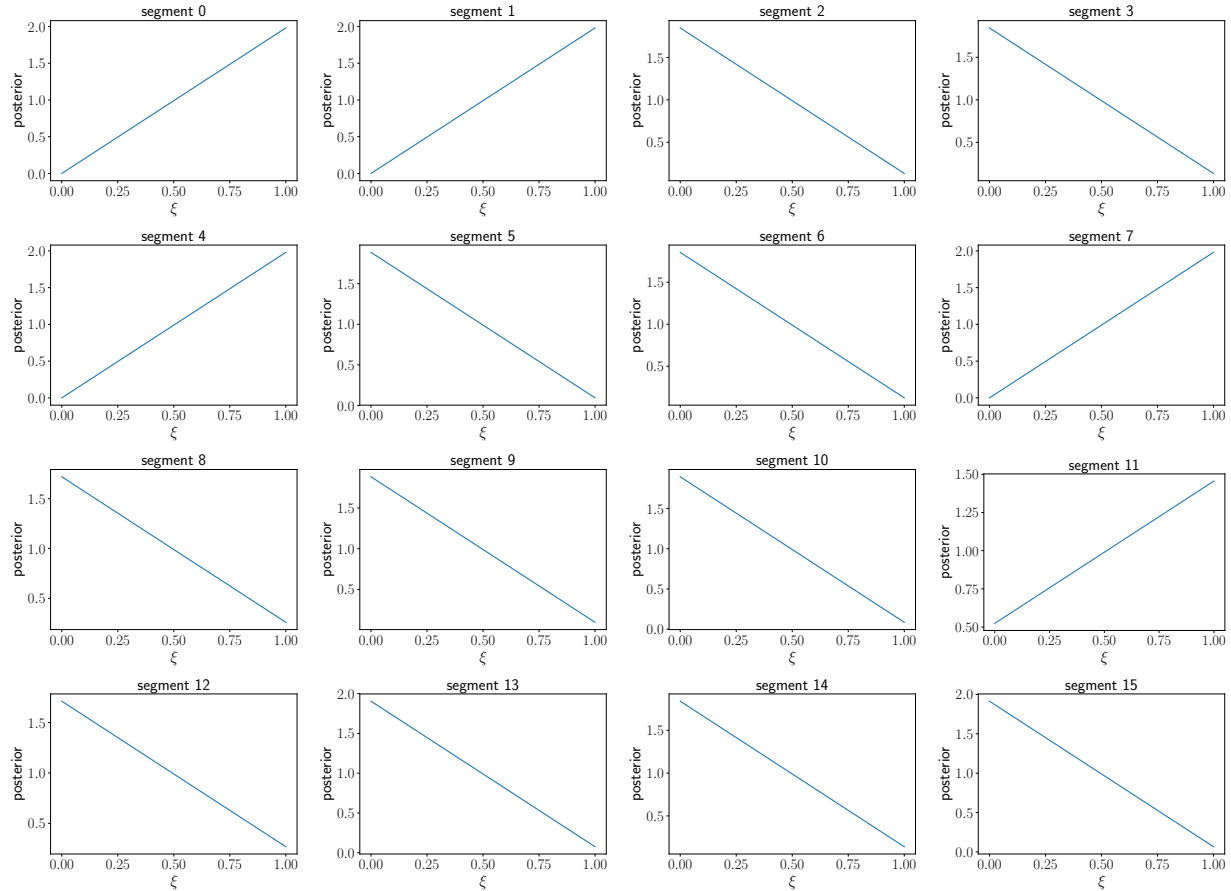


Figure 29: Posterior distributions for ξ for the first 16 segments (first 4 sec) of data. Since the injected signals were relatively large, the posteriors having positive (negative) slope correspond to the segments having (not having) an injected BBH chirp signal.

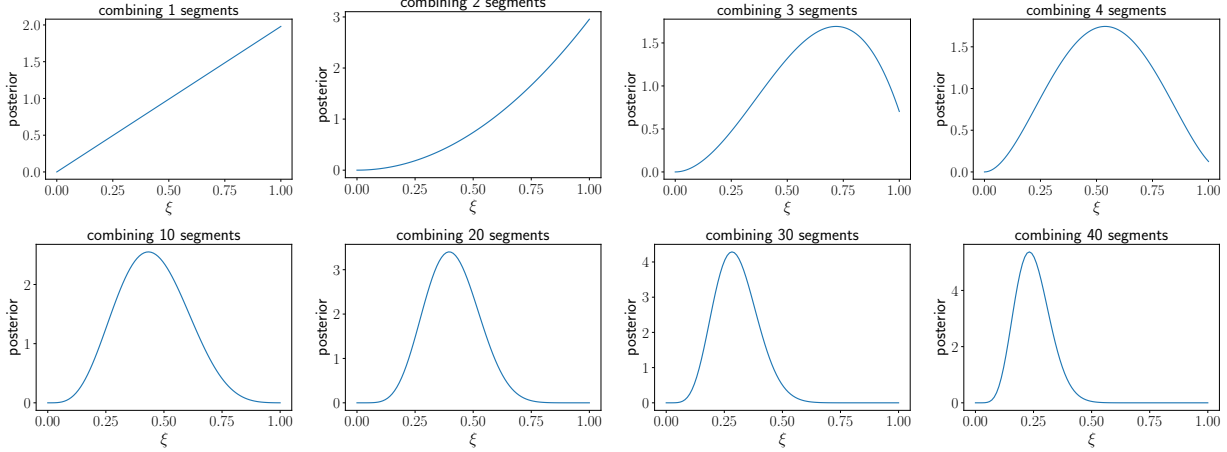


Figure 30: Cumulative posterior distributions for ξ , obtained by combining the likelihood functions for the first n segments of data. The bottom-rightmost plot is also shown in Figure 28.

9.3 Comparison with the standard cross-correlation search

Of course, one can also use the standard cross-correlation method to analyse this simulated data. Although not optimal for a non-continuous background like this, the cross-correlation method performed rather well for this simulation having $\text{SNR}_{\text{CC}} = 8.9$. This should be compared to $\text{SNR}_{\text{bayes}} = 15.3$ for the Bayesian search, where we converted the signal+noise to noise-only Bayes factor $\mathcal{B}_{10}(d)$ to a signal-to-noise ratio using (8.19) and (8.9). So the Bayesian search performed better than the standard cross-correlation search as expected, roughly a factor of two in signal-to-noise ratio for this particular simulation.

More generally, the Bayesian method performs better than the standard cross-correlation method for the BBH background because it properly models the popcorn-like nature of the BBH merger signals. It uses a mixture likelihood, allowing for different probability distributions for those segments that contain a signal and those that do not. The standard cross-correlation method treats all segments on equal footing, looking for excess correlated power which it can ascribe to the signal. So if most of the segments contain only noise, as is the case for BBH merger background, the standard cross-correlation method is going to take longer to build up the signal-to-noise ratio needed to claim detection. The standard cross-correlation method is basically measuring the product of the probability parameter ξ and the cross-correlated power in an individual segment containing a signal. The Bayesian method, on the other hand, is simply measuring ξ , and hence all segments—even those that contain just noise—are providing useful information.

In addition, the Bayesian method incorporates into its signal model the fact that the background is produced by individual BBH mergers, which are described by *deterministic* chirp waveforms (so tracks in time-frequency space). This effectively reduces the time-frequency volume over which the Bayesian method has to search. The standard cross-correlation method, on the other hand, is very much a broadband search, defined by the shape of the power spectral density that one is searching for. By searching over a larger time-frequency volume than it has to, the standard cross-correlation search has to contend with correspondingly more noise.

For these two reasons, one expects the proposed Bayesian search method to be more efficient than the standard cross-correlation method in detecting the popcorn background produced by BBH merger signals. Simulations [47] have shown a reduction in time to detection by roughly a factor

of 1000. This means that when the advanced LIGO and Virgo detectors are operating at design sensitivity, 40 months of observation to detect the BBH background at the 3σ level using the standard cross-correlation method (see Figure 3) is reduced to ~ 1 day using the Bayesian method described here. So we might be detecting this background much sooner than we originally thought.

10 Final thoughts

The purpose of these lecture notes was to introduce the reader to methods used to search for stochastic GW backgrounds. By its very nature, an introduction is necessarily incomplete; not all topics can be discussed. As such, we did not discuss in any detail: (i) searches for stochastic backgrounds using the proposed space-based interferometer LISA, (ii) search methods for anisotropic or unpolarized backgrounds, and (iii) search methods for backgrounds predicted by alternative theories of gravity, etc. The interested reader can find more detail about those topics in [41] and references therein.

Although as of the time of writing these notes (summer 2019) we have not yet detected a stochastic GW background, we know now that such a signal exists, and it's just a matter of time before we reach the sensitivity level needed to make a confident detection. For the GWB produced by stellar-mass BBHs throughout the universe, we expect to reach this level by the time the advanced LIGO and Virgo detectors are operating at design sensitivity (in a couple of years time). But recall that this time-to-detection estimate is conservative, since it assumes that we are using the standard cross-correlation method, which is not optimal for non-continuous backgrounds. As mentioned in Section 9, there is a good chance that we will detect this background earlier using an optimal Bayesian method [47] that properly models the non-continuous, popcorn-like nature of the BBH mergers. But then again, searches using pulsar timing arrays might make the first detection of a stochastic background [46, 42, 49], although for a different class of source—inspiraling SMBHs in the centers of distant galaxies. Either way, it will be an exciting time.

Unlike the detection of the individually resolvable BBH and BNS mergers that advanced LIGO and Virgo has detected, we won't be able to say on one particular day that we've definitely detected a stochastic GW background. Rather we will first see evidence for a background at the 3σ level; and then a year or two later, we will have evidence at the 4 or 5σ level. One of the nice things about stochastic backgrounds is that they are persistent signals (even if popcorn-like), so the longer we observe them, the greater our confidence in detecting them. And once we've confidently detected a stochastic background, the fun part of characterizing what we have seen begins. As mentioned in Section 2, different GW sources will produce different types of backgrounds, so we will need to tease apart their different contributions. And as the sensitivity of GW detectors improve, we will be able to observe additional structure in a background, e.g., anisotropies [14, 27] that were not resolvable before. Needless to say, there is plenty of work and interesting science ahead of us.

Acknowledgements

I acknowledge support from National Science Foundation (NSF) award PHY-1505861; a subaward from the University of Wisconsin-Milwaukee for the NSF NANOGrav Physics Frontier Center (NSF PFC-1430284); a subaward from the University of Minnesota for NASA grant 80NSSC19K0318; and start-up funds from Texas Tech University. I am also grateful to the organizers, fellow lecturers, and of course the students at the 2018 Les Houches Summer School on Gravitational Waves for providing an extremely stimulating environment in which to give these lectures; and I thank the Observatoire Cote D'Azur in Nice, France for its hospitality, where most of these lecture notes

were written. Finally, special thanks goes out to Alex Jenkins for carefully reading through several early drafts of these lecture notes. He provided very helpful feedback and comments that have improved the presentation of the material. (This document has been assigned LIGO Document Control Center number LIGO-P1900196.)

A Exercises

A.1 Rate estimate of stellar-mass binary black hole mergers

Estimate the total rate (number of events per time) of stellar-mass binary black hole mergers throughout the universe by multiplying LIGO's O1 local rate estimate $R_0 \sim 10 - 200 \text{ Gpc}^{-3} \text{ yr}^{-1}$ by the comoving volume out to some large redshift, e.g., $z = 10$. (For this calculation you can ignore any dependence of the rate density with redshift.) You should find a merger rate of ~ 1 per minute to a few per hour. *Hint:* You will need to do numerically evaluate the following integral for proper distance today as a function of source redshift:

$$d_0(z) = \frac{c}{H_0} \int_0^z \frac{dz'}{E(z')} , \quad E(z) \equiv \sqrt{\Omega_m(1+z)^3 + \Omega_\Lambda} , \quad (\text{A.1})$$

with

$$\Omega_m = 0.31 , \quad \Omega_\Lambda = 0.69 , \quad H_0 = 68 \text{ km s}^{-1} \text{ Mpc}^{-1} . \quad (\text{A.2})$$

Doing that integral, you should find what's shown in Figure 31, which you can then evaluate at $z = 10$ to convert R_0 (number of events per comoving volume per time) to total rate (number of events per time) for sources out to redshift $z = 10$.

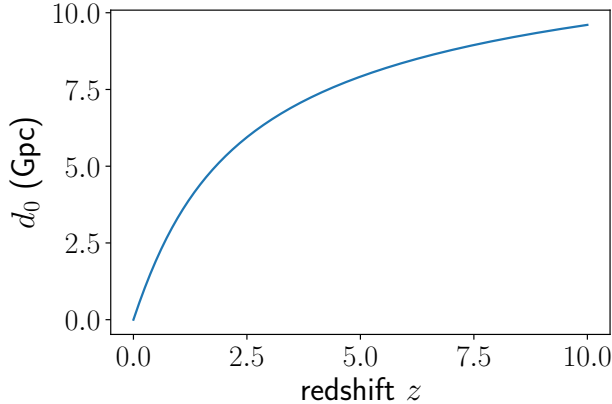


Figure 31

A.2 Relating $S_h(f)$ and $\Omega_{\text{gw}}(f)$

Derive the relationship

$$S_h(f) = \frac{3H_0^2}{2\pi^2} \frac{\Omega_{\text{gw}}(f)}{f^3} \quad (\text{A.3})$$

between the strain power spectral density $S_h(f)$ and the dimensionless fractional energy density spectrum $\Omega_{\text{gw}}(f)$. (*Hint:* You will need to use the various definitions of these quantities and also

$$\rho_{\text{gw}} = \frac{c^2}{32\pi G} \langle \dot{h}_{ab}(t, \vec{x}) \dot{h}^{ab}(t, \vec{x}) \rangle, \quad (\text{A.4})$$

which expresses the energy-density in gravitational-waves to the metric perturbations $h_{ab}(t, \vec{x})$.)

A.3 Cosmology and the “Phinney formula” for astrophysical backgrounds

(a) Using the Friedmann equation

$$\left(\frac{\dot{a}}{a}\right)^2 = H_0^2 \left(\frac{\Omega_m}{a^3} + \Omega_\Lambda\right) \quad (\text{A.5})$$

for a spatially-flat FRW spacetime with matter and cosmological constant, and the relationship

$$1+z = \frac{1}{a(t)}, \quad a(t_0) \equiv 1 \quad (t_0 \equiv \text{today}), \quad (\text{A.6})$$

between redshift z and scale factor $a(t)$, derive

$$\frac{dt}{dz} = -\frac{1}{(1+z)H_0E(z)}, \quad E(z) = \sqrt{\Omega_m(1+z)^3 + \Omega_\Lambda}. \quad (\text{A.7})$$

(b) Using this result for dt/dz , show that

$$\Omega_{\text{gw}}(f) = \frac{f}{\rho_c H_0} \int_0^\infty dz R(z) \frac{1}{(1+z)E(z)} \left(\frac{dE_{\text{gw}}}{df_s} \right) \Big|_{f_s=f(1+z)} \quad (\text{A.8})$$

in terms of the rate density $R(z)$ as measured in the source frame (number of events per comoving volume per time interval in the source frame). (*Hint:* The expression for dt/dz from part (a) will allow you to go from the “Phinney formula” for $\Omega_{\text{gw}}(f)$ written in terms of the number density $n(z)$,

$$\Omega_{\text{gw}}(f) = \frac{1}{\rho_c} \int_0^\infty dz n(z) \frac{1}{1+z} \left(f_s \frac{dE_{\text{gw}}}{df_s} \right) \Big|_{f_s=f(1+z)}, \quad (\text{A.9})$$

to one in terms of the rate density $R(z)$, where $n(z)dz = R(z)|dt|_{t=t(z)}$. Note: Both of the above expressions for $\Omega_{\text{gw}}(f)$ assume that there is only one type of source, described by some set of average source parameters. If there is more than one type of source, one must sum the contributions of each source to $\Omega_{\text{gw}}(f)$.)

A.4 Optimal filtering for the cross-correlation statistic

Verify the form

$$\tilde{Q}(f) \propto \frac{\Gamma_{12}(f)H(f)}{P_1(f)P_2(f)}, \quad (\text{A.10})$$

of the optimal filter function in the weak-signal limit, where $H(f)$ is the assumed spectral shape of the gravitational-wave background, $\Gamma_{12}(f)$ is the overlap function, and $P_1(f)$, $P_2(f)$ are the power spectral densities of the outputs of the two detectors (which are approximately equal to $P_{n_1}(f)$, $P_{n_2}(f)$, respectively). Recall that the optimal filter $\tilde{Q}(f)$ maximizes the signal-to-noise ratio of the

cross-correlation statistic. (*Hint:* Introduce an inner product on the space of functions of frequency $A(f)$, $B(f)$:

$$(A, B) \equiv \int df A(f) B^*(f) P_1(f) P_2(f). \quad (\text{A.11})$$

This inner product has all of the properties of the familiar dot product of vectors in 3-dimensional space. The signal-to-noise ratio of the cross-correlation statistic can be written in terms of this inner product.)

A.5 Maximum-likelihood estimators for single and multiple parameters

(a) Show that the maximum-likelihood estimator \hat{a} of the single parameter a in the likelihood function

$$p(d|a, \sigma) \propto \exp \left[-\frac{1}{2} \sum_{i=1}^N \frac{(d_i - a)^2}{\sigma_i^2} \right] \quad (\text{A.12})$$

is given by the noise-weighted average

$$\hat{a} = \sum_i \frac{d_i}{\sigma_i^2} / \sum_j \frac{1}{\sigma_j^2}. \quad (\text{A.13})$$

(b) Extend the previous calculation to the likelihood

$$p(d|A, C) \propto \exp \left[-\frac{1}{2} (d - MA)^\dagger C^{-1} (d - MA) \right], \quad (\text{A.14})$$

where $A \equiv A_\alpha$ is a vector of parameters, $C \equiv C_{ij}$ is the noise covariance matrix, and $M \equiv M_{i\alpha}$ is the response matrix mapping A_α to data samples, $MA \equiv \sum_\alpha M_{i\alpha} A_\alpha$. For this more general case you should find:

$$\hat{A} = F^{-1} X, \quad (\text{A.15})$$

where

$$F \equiv M^\dagger C^{-1} M, \quad X \equiv M^\dagger C^{-1} d. \quad (\text{A.16})$$

In general, the matrix F (called the *Fisher* matrix) is not invertible, so some sort of regularization is needed to do the matrix inversion.

A.6 Timing-residual response for a 1-arm, 1-way detector

Derive the timing residual response function

$$R^A(f, \hat{k}) = \frac{1}{2} u^a u^b e_{ab}^A(\hat{k}) \frac{1}{i2\pi f} \frac{1}{1 - \hat{k} \cdot \hat{u}} \left[1 - e^{-\frac{i2\pi f L}{c}(1 - \hat{k} \cdot \hat{u})} \right] \quad (\text{A.17})$$

for a single-link (i.e., a one-arm, one-way detector like that for pulsar timing). Here \hat{u} is the direction of propagation of the electromagnetic pulse, and \hat{k} is the direction of propagation of the GW (the direction to the GW source is $\hat{n} \equiv -\hat{k}$, and the direction to the pulsar is $\hat{p} \equiv -\hat{u}$). The origin of coordinates is taken to be at the position of the detector.

A.7 Overlap function for colocated electric dipole antennae

Show that the overlap function for a pair of (short) colocated electric dipole antennae pointing in directions \hat{u}_1 and \hat{u}_2 (Figure 22) is given by

$$\Gamma_{12} \propto \hat{u}_1 \cdot \hat{u}_2 \equiv \cos \zeta \quad (\text{A.18})$$

for the case of an unpolarized, isotropic electromagnetic field. (*Hint:* “short” means that the phase of the electric field can be taken to be constant over of the lengths of the dipole antennae, so that the reponse of antenna $I = 1, 2$ to the field is given by $r_I(t) = \hat{u}_I \cdot \vec{E}(t, \vec{x}_0)$, where \vec{x}_0 is the common location of the two antenna.)

A.8 Maximum-likelihood estimators for the standard cross-correlation statistic

Verify that

$$\hat{C}_{11} \equiv \frac{1}{N} \sum_{i=1}^N d_{1i}^2, \quad \hat{C}_{22} \equiv \frac{1}{N} \sum_{i=1}^N d_{2i}^2, \quad \hat{C}_{12} \equiv \frac{1}{N} \sum_{i=1}^N d_{1i} d_{2i} \quad (\text{A.19})$$

are maximum-likelihood estimators of

$$S_1 \equiv S_{n_1} + S_h, \quad S_2 \equiv S_{n_2} + S_h, \quad S_h, \quad (\text{A.20})$$

for the case of N samples of a white GWB in uncorrelated white detector noise, for a pair of colocated and coaligned detectors. Recall that the likelihood function is

$$p(d|S_{n_1}, S_{n_2}, S_h) = \frac{1}{\sqrt{\det(2\pi C)}} \exp \left[-\frac{1}{2} d^T C^{-1} d \right], \quad (\text{A.21})$$

where

$$C = \begin{bmatrix} (S_{n_1} + S_h) \mathbf{1}_{N \times N} & S_h \mathbf{1}_{N \times N} \\ S_h \mathbf{1}_{N \times N} & (S_{n_2} + S_h) \mathbf{1}_{N \times N} \end{bmatrix} \quad (\text{A.22})$$

and

$$d^T C^{-1} d \equiv \sum_{I,J=1}^2 \sum_{i,j=1}^N d_{Ii} (C^{-1})_{Ii,Jj} d_{Jj}. \quad (\text{A.23})$$

A.9 Derivation of the maximum-likelihood ratio detection statistic

Verify that twice the log of the maximum-likelihood ratio for the standard stochastic likelihood function goes like the square of the (power) signal-to-noise ratio,

$$2 \ln \Lambda_{\text{ML}}(d) \simeq \frac{\hat{C}_{12}^2}{\hat{C}_{11} \hat{C}_{22}/N}, \quad (\text{A.24})$$

in the weak-signal approximation. (*Hint:* For simplicity, do the calculation in the context of N samples of a white GWB in uncorrelated white detector noise, for a pair of colocated and coaligned detectors, using the results of Exercise A.8.)

A.10 Standard likelihood marginalizing over stochastic signal prior

Derive the standard form of the likelihood function for stochastic background searches

$$p(d|S_{n_1}, S_{n_2}, S_h) = \frac{1}{\sqrt{\det(2\pi C)}} \exp \left[-\frac{1}{2} \sum_{I,J=1}^2 d_I (C^{-1})_{IJ} d_J \right], \quad (\text{A.25})$$

where

$$C \equiv \begin{bmatrix} S_{n_1} + S_h & S_h \\ S_h & S_{n_2} + S_h \end{bmatrix}, \quad (\text{A.26})$$

by marginalizing

$$p_n(d - h|S_{n_1}, S_{n_2}) = \frac{1}{2\pi\sqrt{S_{n_1}S_{n_2}}} \exp \left[-\frac{1}{2} \left\{ \frac{(d_1 - h)^2}{S_{n_1}} + \frac{(d_2 - h)^2}{S_{n_2}} \right\} \right] \quad (\text{A.27})$$

over the signal samples h for the *stochastic* signal prior

$$p(h|S_h) = \frac{1}{\sqrt{2\pi S_h}} \exp \left[-\frac{1}{2} \frac{h^2}{S_h} \right]. \quad (\text{A.28})$$

In other words, show that

$$p(d|S_{n_1}, S_{n_2}, S_h) = \int_{-\infty}^{\infty} dh p_n(d - h|S_{n_1}, S_{n_2}) p(h|S_h). \quad (\text{A.29})$$

(*Hint:* You'll have to complete the square in the argument of the exponential in the marginalization integral.)

References

- [1] Abbott, B. P. et al. (Virgo, LIGO Scientific), “GW150914: Implications for the stochastic gravitational wave background from binary black holes”, *Phys. Rev. Lett.*, **116**(13), 131102 (2016). [DOI], [arXiv:1602.03847 [gr-qc]].
- [2] Abbott, B. P. et al., “Observation of Gravitational Waves from a Binary Black Hole Merger”, *Physical Review Letters*, **116**(6), 061102 (February 2016). [DOI], [ADS], [arXiv:1602.03837 [gr-qc]].
- [3] Abbott, B. P. et al., “GW170817: Observation of Gravitational Waves from a Binary Neutron Star Inspiral”, *Phys. Rev. Lett.*, **119**(16), 161101 (Oct 2017). [DOI], [ADS], [arXiv:1710.05832 [gr-qc]].
- [4] Abbott, B. P. et al., “GW170817: Implications for the Stochastic Gravitational-Wave Background from Compact Binary Coalescences”, *Phys. Rev. Lett.*, **120**(9), 091101 (Mar 2018). [DOI], [ADS], [arXiv:1710.05837 [gr-qc]].
- [5] Adams, Matthew R. and Cornish, Neil J., “Discriminating between a Stochastic Gravitational Wave Background and Instrument Noise”, *Phys. Rev.*, **D82**, 022002 (2010). [DOI], [arXiv:1002.1291 [gr-qc]].
- [6] Adams, Matthew R. and Cornish, Neil J., “Detecting a Stochastic Gravitational Wave Background in the presence of a Galactic Foreground and Instrument Noise”, *Phys. Rev.*, **D89**(2), 022001 (2014). [DOI], [arXiv:1307.4116 [gr-qc]].
- [7] Allen, B., “The Stochastic Gravity-Wave Background: Sources and Detection”, in Marck, J.-A. and Lasota, J.-P., eds., *Relativistic Gravitation and Gravitational Radiation*, p. 373, (1997). [ADS], [gr-qc/9604033].
- [8] Allen, B. and Ottewill, A. C., “Detection of anisotropies in the gravitational-wave stochastic background”, *Phys. Rev. D*, **56**, 545–563 (July 1997). [DOI], [ADS], [gr-qc/9607068].
- [9] Allen, Bruce and Romano, Joseph D., “Detecting a stochastic background of gravitational radiation: Signal processing strategies and sensitivities”, *Phys. Rev. D*, **59**(10), 102001 (May 1999). [DOI], [ADS], [arXiv:gr-qc/9710117 [gr-qc]].
- [10] Bender, P. L. and Hils, D., “Confusion noise level due to galactic and extragalactic binaries”, *Classical and Quantum Gravity*, **14**, 1439–1444 (June 1997). [DOI], [ADS].
- [11] Chamberlin, S. J. and Siemens, X., “Stochastic backgrounds in alternative theories of gravity: Overlap reduction functions for pulsar timing arrays”, *Phys. Rev. D*, **85**(8), 082001 (April 2012). [DOI], [ADS], [arXiv:1111.5661 [astro-ph.HE]].
- [12] Christensen, N., “Optimal detection strategies for measuring the stochastic gravitational radiation background with laser interferometric antennas”, *Phys. Rev. D*, **55**, 448–454 (January 1997). [DOI], [ADS].
- [13] Coughlin, Michael W. et al., “Subtraction of correlated noise in global networks of gravitational-wave interferometers” (2016). [arXiv:1606.01011 [gr-qc]].

- [14] Cusin, Giulia, Pitrou, Cyril and Uzan, Jean-Philippe, “Anisotropy of the astrophysical gravitational wave background: Analytic expression of the angular power spectrum and correlation with cosmological observations”, *Phys. Rev. D*, **96**(10), 103019 (Nov 2017). [DOI], [ADS], [arXiv:1704.06184 [astro-ph.CO]].
- [15] Detweiler, S., “Pulsar timing measurements and the search for gravitational waves”, *ApJ*, **234**, 1100–1104 (December 1979). [DOI], [ADS].
- [16] Dicke, R. H., Peebles, P. J. E., Roll, P. G. and Wilkinson, D. T., “Cosmic Black-Body Radiation.”, *ApJ*, **142**, 414–419 (July 1965). [DOI], [ADS].
- [17] Estabrook, F. B., Tinto, Massimo and Armstrong, J. W., “Time delay analysis of LISA gravitational wave data: Elimination of spacecraft motion effects”, *Phys. Rev.*, **D62**, 042002 (2000). [DOI].
- [18] Flanagan, Éanna É., “Sensitivity of the Laser Interferometer Gravitational Wave Observatory to a stochastic background, and its dependence on the detector orientations”, *Phys. Rev. D*, **48**, 2389 (1993).
- [19] Gair, J., Romano, J. D., Taylor, S. and Mingarelli, C. M. F., “Mapping gravitational-wave backgrounds using methods from CMB analysis: Application to pulsar timing arrays”, *Phys. Rev. D*, **90**(8), 082001 (October 2014). [DOI], [ADS], [arXiv:1406.4664 [gr-qc]].
- [20] Gair, J. R., Romano, J. D. and Taylor, S. R., “Mapping gravitational-wave backgrounds of arbitrary polarisation using pulsar timing arrays”, *Phys. Rev. D*, **92**(10), 102003 (November 2015). [DOI], [ADS], [arXiv:1506.08668 [gr-qc]].
- [21] Gregory, Phil C., *Bayesian Logical Data Analysis for the Physical Sciences: A Comparative Approach with Mathematica Support*, (Cambridge University Press, Cambridge, UK, New York, NY, 2005).
- [22] Grishchuk, L. P., “Primordial gravitons and possibility of their observation”, *Journal of Experimental and Theoretical Physics Letters*, **23**, 293 (1976).
- [23] Hartle, James B., *Gravity: An Introduction to Einstein’s General Relativity*, (Addison Wesley, 2002).
- [24] Hellings, R. W. and Downs, G. S., “Upper limits on the isotropic gravitational radiation background from pulsar timing analysis”, *ApJ*, **265**, L39–L42 (1983).
- [25] Helstrom, Carl W., *Statistical Theory of Signal Detection, 2nd edition*, (Pergamon Press, Oxford, London, Edinburgh, New York, Toronto, Sydney, Paris, Braunschweig, 1968).
- [26] Jenet, F. A. and Romano, J. D., “Understanding the gravitational-wave Hellings and Downs curve for pulsar timing arrays in terms of sound and electromagnetic waves”, *American Journal of Physics*, **83**, 635–645 (July 2015). [DOI], [ADS], [arXiv:1412.1142 [gr-qc]].
- [27] Jenkins, Alexander C. and Sakellariadou, Mairi, “Anisotropies in the stochastic gravitational-wave background: Formalism and the cosmic string case”, *Phys. Rev. D*, **98**(6), 063509 (Sep 2018). [DOI], [ADS], [arXiv:1802.06046 [astro-ph.CO]].
- [28] Kogut, A. et al., “The Primordial Inflation Explorer (PIXIE): a nulling polarimeter for cosmic microwave background observations”, *Journal of Cosmology and Astro-Particle Physics*, **2011**(7), 025 (Jul 2011). [DOI], [ADS], [arXiv:1105.2044 [astro-ph.CO]].

- [29] Kolb, E. W. and Turner, M., *The Early Universe*, (Addison Wesley, 1990).
- [30] Lee, K., Jenet, F. and Price, R., “Detecting Gravitational Waves of Alternative Theories Using Pulsar Timing”, in *American Astronomical Society Meeting Abstracts*, Bulletin of the American Astronomical Society, 39, 102.07, (December 2007). [ADS].
- [31] Maggiore, M., “Gravitational wave experiments and early universe cosmology”, *Phys. Rep.*, **331**, 283–367 (July 2000). [DOI], [ADS], [gr-qc/9909001].
- [32] Masi, S., “The BOOMERanG experiment and the curvature of the universe”, *Progress in Particle and Nuclear Physics*, **48**(1), 243–261 (Jan 2002). [DOI], [ADS], [arXiv:astro-ph/0201137 [astro-ph]].
- [33] Mingarelli, C. M. F., Sidery, T., Mandel, I. and Vecchio, A., “Characterizing gravitational wave stochastic background anisotropy with pulsar timing arrays”, *Phys. Rev. D*, **88**(6), 062005 (September 2013). [DOI], [ADS], [arXiv:1306.5394 [astro-ph.HE]].
- [34] Misner, C. W., Thorne, K. S. and Wheeler, J. A., *Gravitation*, (W.H. Freeman and Company, San Francisco, 1973).
- [35] Parida, Abhishek, Mitra, Sanjit and Jhingan, Sanjay, “Component Separation of a Isotropic Gravitational Wave Background”, *Journal of Cosmology and Astroparticle Physics*, **2016** (10 2015). [DOI].
- [36] Penzias, A. A. and Wilson, R. W., “A Measurement of Excess Antenna Temperature at 4080 Mc/s.”, *ApJ*, **142**, 419–421 (July 1965). [DOI], [ADS].
- [37] Peters, P. C. and Mathews, J., “Gravitational Radiation from Point Masses in a Keplerian Orbit”, *Phys. Rev.*, **131**, 435–440 (Jul 1963). [DOI]URL:
<https://link.aps.org/doi/10.1103/PhysRev.131.435>.
- [38] Phinney, E. S., “A Practical Theorem on Gravitational Wave Backgrounds”, *arXiv e-prints*, astro-ph/0108028 (Aug 2001). [ADS], [arXiv:astro-ph/0108028 [astro-ph]].
- [39] Planck Collaboration et al., “Planck 2018 results. VII. Isotropy and Statistics of the CMB”, *arXiv e-prints*, arXiv:1906.02552 (Jun 2019). [ADS], [arXiv:1906.02552 [astro-ph.CO]].
- [40] Prince, Thomas A., Tinto, Massimo, Larson, Shane L. and Armstrong, J. W., “The LISA optimal sensitivity”, *Phys. Rev.*, **D66**, 122002 (2002). [DOI], [arXiv:gr-qc/0209039 [gr-qc]].
- [41] Romano, Joseph D. and Cornish, Neil J., “Detection methods for stochastic gravitational-wave backgrounds: a unified treatment”, *Living Reviews in Relativity*, **20**(1), 2 (Apr 04, 2017). [DOI]URL:
<https://doi.org/10.1007/s41114-017-0004-1>.
- [42] Rosado, Pablo A., Sesana, Alberto and Gair, Jonathan, “Expected properties of the first gravitational wave signal detected with pulsar timing arrays”, *Mon. Not. Roy. Astron. Soc.*, **451**(3), 2417–2433 (2015). [DOI], [arXiv:1503.04803 [astro-ph.HE]].
- [43] Ryden, B., *Introduction to cosmology*, (Cambridge University Press, 2016)URL:
<http://www.cambridge.org/de/academic/subjects/astronomy/cosmology-and-relativity/introduction-cosmology-2nd-edition-1?format=HB>.

- [44] Sazhin, M. V., “Opportunities for detecting ultralong gravitational waves”, *Soviet Ast.*, **22**, 36–38 (February 1978). [ADS].
- [45] Seljak, Uros and Zaldarriaga, Matias, “Signature of gravity waves in polarization of the microwave background”, *Phys. Rev. Lett.*, **78**, 2054–2057 (1997). [DOI], [arXiv:astro-ph/9609169 [astro-ph]].
- [46] Siemens, X., Ellis, J., Jenet, F. and Romano, J. D., “The stochastic background: scaling laws and time to detection for pulsar timing arrays”, *Classical and Quantum Gravity*, **30**(22), 224015 (November 2013). [DOI], [ADS], [arXiv:1305.3196 [astro-ph.IM]].
- [47] Smith, Rory and Thrane, Eric, “Optimal Search for an Astrophysical Gravitational-Wave Background”, *Phys. Rev. X*, **8**, 021019 (Apr 2018). [DOI]URL: <https://link.aps.org/doi/10.1103/PhysRevX.8.021019>.
- [48] Smoot, G. F. et al., “Structure in the COBE Differential Microwave Radiometer First-Year Maps”, *ApJ*, **396**, L1 (Sep 1992). [DOI], [ADS].
- [49] Taylor, S. R., Vallisneri, M., Ellis, J. A., Mingarelli, C. M. F., Lazio, T. J. W. and van Haasteren, R., “Are We There Yet? Time to Detection of Nanohertz Gravitational Waves Based on Pulsar-timing Array Limits”, *ApJ*, **819**, L6 (March 2016). [DOI], [ADS], [arXiv:1511.05564 [astro-ph.IM]].
- [50] The LIGO Scientific Collaboration et al., “Binary Black Hole Mergers in the first Advanced LIGO Observing Run”, *ArXiv e-prints* (June 2016). [ADS], [arXiv:1606.04856 [gr-qc]].
- [51] The LIGO Scientific Collaboration et al., “GWTC-1: A Gravitational-Wave Transient Catalog of Compact Binary Mergers Observed by LIGO and Virgo during the First and Second Observing Runs”, *arXiv e-prints*, arXiv:1811.12907 (Nov 2018). [ADS], [arXiv:1811.12907 [astro-ph.HE]].
- [52] Thrane, E., Ballmer, S., Romano, J. D., Mitra, S., Talukder, D., Bose, S. and Mandic, V., “Probing the anisotropies of a stochastic gravitational-wave background using a network of ground-based laser interferometers”, *Phys. Rev. D*, **80**(12), 122002 (December 2009). [DOI], [ADS], [arXiv:0910.0858 [astro-ph.IM]].
- [53] Thrane, E., Christensen, N. and Schofield, R. M. S., “Correlated magnetic noise in global networks of gravitational-wave detectors: Observations and implications”, *Phys. Rev. D*, **87**, 123009 (Jun 2013). [DOI]URL: <http://link.aps.org/doi/10.1103/PhysRevD.87.123009>.
- [54] Thrane, E., Christensen, N., Schofield, R. M. S. and Effler, A., “Correlated noise in networks of gravitational-wave detectors: Subtraction and mitigation”, *Phys. Rev. D*, **90**, 023013 (Jul 2014). [DOI]URL: <http://link.aps.org/doi/10.1103/PhysRevD.90.023013>.
- [55] “<http://bicepkeck.org/>”.
- [56] “http://litebird.jp/eng/?page_id=2”.
- [57] “<https://github.com/josephromano/leshouches/tree/master/code>”.
- [58] “<https://gwcenter.icrr.u-tokyo.ac.jp/en/>”.

- [59] “<https://lambda.gsfc.nasa.gov/product/cobe/>”.
- [60] “<https://map.gsfc.nasa.gov>”.
- [61] “<https://www.cosmos.esa.int/web/planck>”.
- [62] “<https://www.elisascience.org>”.
- [63] “<https://www.gw-openscience.org>”.
- [64] “<http://www.gw-indigo.org>”.
- [65] “<http://www.ligo.caltech.edu/>”.
- [66] “<http://www.virgo-gw.eu>”.
- [67] Wainstein, L. A. and Zubakov, V. D., *Extractions of Signals from Noise*, (Dover Publications Inc., 1971).